POLITECNICO DI TORINO
Repository ISTITUZIONALE

Graphene, Graphene Oxide and Carbon Nanotubes in Raman Spectroscopy

Original
Graphene, Graphene Oxide and Carbon Nanotubes in Raman Spectroscopy / Sparavigna, A.C.. - In: INTERNATIONAL JOURNAL OF SCIENCES. - ISSN 2305-3925. - 13:07(2024), pp. 1-26. [10.18483/ijsci.2773]

Availability:
This version is available at: 11583/2990341 since: 2024-07-04T05:51:43Z

Publisher:
Alkhaer Publications

Published
DOI:10.18483/ijsci.2773

Terms of use:

This article is made available under terms and conditions as specified in the corresponding bibliographic description in the repository

Publisher copyright

(Article begins on next page)

10 November 2026

International Journal of Sciences

Research Article Volume 13 – July 2024 (07)

Graphene, Graphene Oxide and Carbon Nanotubes in Raman Spectroscopy

Amelia Carolina Sparavigna[1]

[1]Department of Applied Science and Technology, Polytechnic University of Turin, Italy

Abstract: In previous discussions we have considered the Raman spectra of specific carbon-based materials, such as diamond, graphite, and the biochar resulting from pyrolysis of biomass. We have shown how spectra can be decomposed, according to the intended number of components and the proper line shapes. Here, we approach the Raman spectra of graphene and graphene oxide, to understand how many components are required to interpret the related fingerprints. Besides graphene and graphene oxides, here we also review some literature about the Raman spectroscopy of carbon nanotubes, focusing especially on the line shapes. As shown by literature, the Raman spectra are able of giving information on the nature of nanotubes (metallic or semiconducting) and if they are single- or multi-walled structures. We will find that the Raman spectroscopy is able of investigating even a single nanotube. It will be stressed the role of curvature in breaking the symmetry of carbon layers, to produce the observed Raman bands. In particular, the existence of Breit-Wigner-Fano lines will be investigated.

Keywords: Raman Spectroscopy, Spectrum Decomposition, q-Gaussian Tsallis Lines, Graphene, Graphene Oxide, Carbo Nanotubes, Carbon-based Materials

Introduction

The modern Raman spectroscopy is based on the photons scattered by a sample when a laser light shines on it. In the inelastic scattering processes, the emitted photons have a frequency shift, the Raman shift, which is producing the "fingerprint" typical of the investigated material. To the best of my knowledge, the first use of the term "fingerprint" for Raman spectroscopy was in the article by Fenske et al., 1947, about the Raman spectra of hydrocarbons. From that time on, the points of identification, such as the positions of peaks, shoulders and valleys have been considered to constitute the characteristic spectral pattern, that is, the "fingerprint" of a given material.

For the carbon-based materials, the Raman spectroscopy is "a particularly well-suited technique" (Zhang et al., 2022), due to the "*long-range* crystalline vibrations and *short-range* molecular vibrations of carbon species", which are producing, for the different materials, their characteristic spectral fingerprints. According to Zhang and coworkers, these fingerprints allow identifying the "specific carbon materials including graphite, diamond, graphene, carbon nanotubes, fullerene, and amorphous carbon". To these materials, we must also add the recent studies on "graphene, bilayer graphene, and two-dimensional graphene heterostructures" (Zhang et al., 2022, Mu and Sun, 2020, Cui and Sun, 2021).

We have already discussed diamond and graphite Raman spectra in the framework of their decomposition in q-Gaussian Tsallis functions. Diamond has a Raman peak at 1332 cm^{-1}, corresponding to the vibration of its two Bravais lattices of carbon atoms with respect to each other (Krishnan, 1945). The crystalline graphite has a G peak at 1582 cm^{-1} and a G' (or 2D) peak at 2700 cm^{-1} (Malard et al., 2009). In other carbonaceous materials, such as soot, kerogen, and biochar, besides the G band we find the D1, D2, D3 and D4 bands mentioned by Beyssac et al., 2002, and Sadezky et al., 2005. In Claramunt et al., 2015, we can find a different notation where D is D1, D2 is D', D3 is D'' and D4 is D*. In Sousa et al., 2020, a further D5 component is used (see for instance the Raman spectrum decomposition in their Figure 2). Sadezky and coworkers give the following Raman shifts (cm^{-1}): ~1580 (G), ~1350 (D1), ~1620 (D2), ~1500 (D3), ~1200 (D4). Let us add ~1700 (D5), according to Sousa et al., 2020.

Here, our aim is that of showing spectra of graphene and graphene oxide, with respect to the graphite spectrum, to understand how many components are required to interpret the fingerprints. Graphene is a two-dimensional honeycomb lattice of carbon atoms that is widely considered for theoretical and applies studies, and for its technological potentials. Raman spectroscopy is considered suitable to characterize it and its related materials (Childres et al., 2013). "A large amount of information such as disorder, edge and grain boundaries, thickness, doping, strain and thermal conductivity of graphene" can be obtained from the spectrum recorded under different physical conditions, as discussed by Childres and coworkers. It means that Raman fingerprints must be able to give the proper information, when decomposed in a convenient manner.

Comparing graphene, defective graphene and graphite spectra

In Ott and Ferrari, 2024, we can find a concise

This article is published under the terms of the Creative Commons Attribution License 4.0
Author(s) retain the copyright of this article. Publication rights with Alkhaer Publications.
Published at: http://www.ijsciences.com/pub/issue/2024-07/
DOI: 10.18483/ijSci.2773; Online ISSN: 2305-3925; Print ISSN: 2410-4477

Amelia Carolina Sparavigna (Correspondence)
+

overview of light scattering processes, especially of the Raman scattering process in graphene. We can see how the Raman peaks are generated by the presence of the optical phonons according to their dispersions in the Brillouin zone. We can also appreciate that the Raman spectrum is sensitive to the number of graphene layers, to the presence of defects and to the straining and doping of it. Therefore, we can find reiterated that the Raman technique "can give insight in the material's quality, the number of layers, and is sensitive to any changes in electric or magnetic fields, band structure and temperature, making it ideal to probe layered materials" (Ott and Ferrari, 2024).

The Fig.3 in Ott and Ferrari illustrates the modes and phonon dispersions for a single layer graphene, whereas in the Fig.4 we can see the Raman spectra of graphite, and pristine and defective graphene. The peaks in the spectra are described in the following manner. "The G peak 1580 cm^{-1} arises from an E_{2g} phonon stemming from the Γ-point, ... The D peak, corresponding to an A_{1g} phonon ..., is due to the breathing mode of six-atom rings and requires a defect for its activation (Ferrari and Robertson, 2000; Thomsen and Reich, 2000; Tuinstra and Koenig, 1970) to fulfill the fundamental Raman selection rule" (Ott and Ferrari, 2024). This peak is activated by a process involving a transverse optical (TO) phonon at the K point. Similarly, another resonance scattering process at K or K' produces the defect-activated D' peak. The combination D+D' is also present. Peaks 2D and 2D' are the second order modes of D and D', "where the momentum conservation is fulfilled by [the] scattering of two phonons with opposite wave vectors". Consequently, defects are not required for their activation and these peaks "are always present in the Raman spectrum of graphene" (Ott and Ferrari, 2024, Ferrari et al., 2006, Basko et al., 2009). Moreover, the G peak is the only peak in graphene Raman spectrum fulfilling "the fundamental Raman selection rule directly, as its origin is at the center of the Brillouin zone where **q** = 0" (Ott and Ferrari, 2024).

Looking at the Figure 4 by Ott and Ferrari we can see that graphite and pristine graphene have the same peaks with differences in intensity and presence of shoulders. Here in our Figure 1, we propose a sketch accordingly.

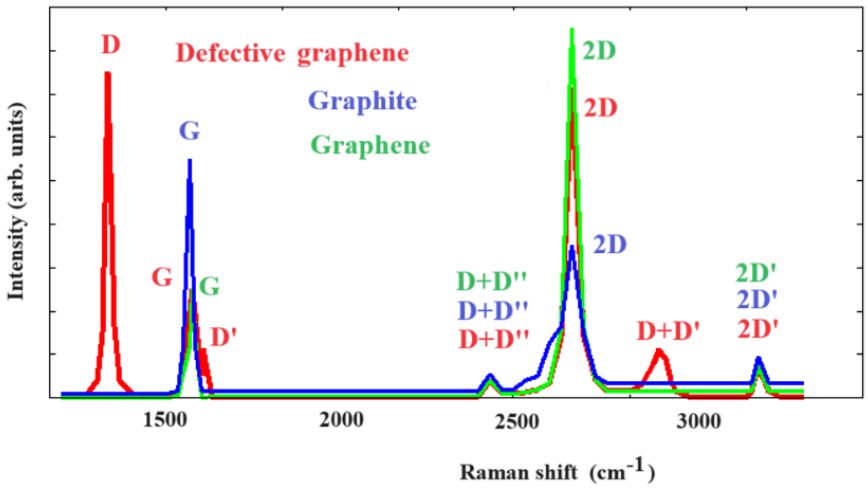

Fig. 1: A sketch of the Raman spectra of pristine Graphene (green), Defective graphene (red) and Graphite (blue) according to the spectra proposed in the Figure 4 by Ott and Ferrari, 2024. We can see that the peaks G, D+D'', 2D and 2D' are present in the three spectra. Peaks D, shoulder D' and peak D+D' are present in the defective graphene.

According to Childres et al., 2013, in graphene, "the Stokes phonon energy shift caused by laser excitation creates two main peaks in the Raman spectrum: G (1580 cm^{-1}), a primary in-plane vibrational mode, and 2D (2690 cm^{-1}), a second-order overtone of a different in plane vibration" [Childres et al. mentioning Saito et al., 2011]. Moreover, we have the D peak (1350 cm^{-1}); as stressed by Childres and coworkers, the D and 2D peak positions are dispersive, and therefore they are dependent on the laser excitation energy (Ferrari, 2007). The given positions are for spectra excited by a 532 nm laser. Due to the presence of interactions between the layers of AB-stacked graphene, "as the number of graphene layers increases, the spectrum will change from that of single-layer graphene", and therefore we have a "splitting of the 2D peak into an increasing number of modes" (Childres et al., mentioning Ferrari et al., 2006). Moreover, the G peak is subjected to a small red shift according to the increased number of layers (Childres et al., 2013, Gupta et al., 2006). Consequently, in the case of AB-stacked graphene, the ratio of peak intensities, I_{2D}/I_G can be related to the number of layers, "as well as the position and shape of these peaks" (Childres et al., 2013, mentioning Ferrari et al., 2006).

The ratio I_D/I_G of the intensities of the D and G peaks is featuring the level of disorder in graphene. However, this increase of disorder is characterized by

two regimes displayed by I_D/I_G. "There is a regime of *low* defect density, where I_D/I_G will increase as a higher defect density creates more elastic scattering" (Childres et al., 2013); however, we have also a "regime of *high* defect density, at which point I_D/I_G will begin to decrease as an increasing defect density results in a *more amorphous carbon structure, attenuating all Raman peaks* [as told by Lucchese, et al., 2010]"; Childres and coworkers, referring to Saito et al., 2011, consider these two regimes featuring "nanocrystalline graphite" and "mainly sp^2 amorphous carbon" phases, respectively. To characterize the disorder, we find also used the L_D length, that is, the average distance between defects, estimated by means of the Raman spectroscopy. In the Figure 3 by Childres and coworkers it is shown the Raman spectrum of graphene irradiated by electron beam, which is "showing significant D, D' and D+G disorder peaks. The concentration of disorder can be extracted from the intensity ratio I_D/I_G".

For what is regarding the graphene edges, "a *strong D peak* will appear near armchair edges using an excitation laser *polarized* in a direction parallel to the line of the edge. This effect is significantly smaller for zigzag edges". It follows in the Childres and coworkers' article a discussion about the optical phonons active in armchair and zigzag edges. From the article, it seems that polarized Raman spectroscopy is relevant for graphene and related materials, and in fact we can find this spectroscopy mentioned by Wu et al., 2018, and Li et al., 2023.

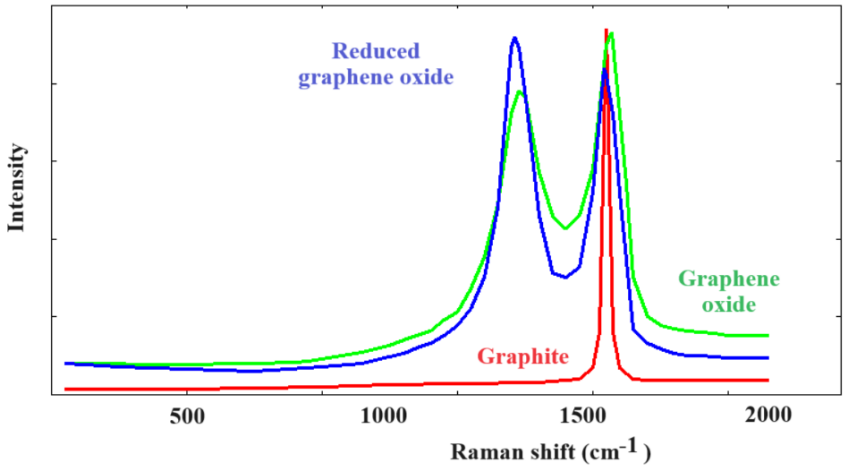

Fig.2: In Childres et al., 2013, we can find reproduced, in their Figure 5, the Raman spectra of graphite (red), graphene oxide (green) and reduced graphene oxide (blue), as given by Stankovich et al., 2007.

Introducing graphene oxide and reduced graphene oxide

In the Fig.5 by Childres et al., 2013, we can find reproduced the Raman spectra of SP-1 grade graphite, graphene oxide and reduced graphene oxide as given by Stankovich et al., 2007. Let us consider this work. Given the Stankovich and coworkers' interest in graphene-based materials, the researchers "set out to develop a general and reproducible approach for the preparation of graphene sheets from graphite". The researchers decided to start from the graphite oxide (GO) "as one possible route". The route proposes a complete exfoliation of GO into individual GO sheets, which are reduced to obtain individual graphene-like sheets (Stankovich et al., 2006). The reduction of exfoliated GO sheets is made by using hydrazine. Stankovich and coworkers characterized the resulting material, presenting "evidence to support the claim that GO can be completely exfoliated into individual graphene oxide sheets and that chemical reduction of such sheets can furnish graphene-like sheets. GO is produced by the oxidative treatment of graphite via one of three principal methods developed by Brodie, 1860, Hummers and Offeman, 1958, and Staudenmeier, 1898, respectively" (Stankovich et al., 2007). According to Stankovich and coworkers, 2007, and references therein, GO is made of oxidized graphene sheets. These sheets have the basal planes "decorated mostly with epoxide and hydroxyl groups, in addition to carbonyl and carboxyl groups located presumably at the edges (Lerf–Klinowski model)" (Stankovich et al., 2006). About this model see, for instance, the figure in Siklitskaya et al., 2021. The presence of oxygen functionalities is rendering the GO layers hydrophilic so that we can have water molecules "readily intercalate into the interlayer galleries. GO can therefore be also thought of as a *graphite-type intercalation compound* – as discussed by Stankovich and coworkers - with both covalently bound oxygen and non-covalently bound water between the carbon layers". A rapid heating of GO is producing delamination, because of the intercalated water evaporation and evolution of gases from pyrolysis (Stankovich et al., 2007, Schniepp et al., 2006). Being GO an electrical insulator, it cannot be used in his natural form for conductive nanomaterials. However, Stankovich and coworkers note that electrical conductivity of GO "can be restored close to the level of graphite by chemical reduction" (Stankovich et al., 2006, and references therein).

Among the examined chemical reducing agents, hydrazine hydrate turned out to be the best, "in producing very thin graphene-like sheets".

About Raman peaks, Stankovich and coworkers note that the changes in the processing of pristine graphite into reduced GO are evidenced by the related Raman spectra. The researchers show the spectra that we sketched in our Figure 2. The given description is as follow: the pristine graphite spectrum has a prominent G peak at 1581 cm^{-1}, coming from the first-order scattering E_{2g} mode (Tuinstra and Koenig, 1970). The GO Raman spectrum has the G band *broadened and shifted* to 1594 cm^{-1}. The D band (1363 cm^{-1}) "becomes prominent, indicating the reduction in size of the in-plane sp^2 domains, possibly due to the extensive oxidation" (Stankovich et al., 2006). The rGO (reduced GO) Raman spectrum has G and D bands, with peaks at 1584 and 1352 cm^{-1}, respectively, "with an increased D/G intensity ratio compared to that in GO. This change suggests a decrease in the average size of the sp^2 domains upon reduction of the exfoliated GO (Stankovich et al. mentioning Tuinstra and Koenig, 1970), and can be explained if *new graphitic domains* were created that are smaller in size to the ones present in GO before reduction, but more numerous in number" (Stankovich et al., 2007).

In the Introduction we have mentioned the work by Claramunt et al., 2015, which is regarding the Raman spectroscopy of GO and rGO. Claramunt and coworkers remember that Brodie, Staudenmaier, Hummers and Offeman proposed GO "as a carbon compound where oxygen functional groups are attached at carbon atoms within the hexagonal plane". Accordingly, "GO consists of two main regions constituted by hydrophobic π-conjugated C-sp^2 and the C-sp^3 domains. The latter are mainly constituted by alcohol and epoxy groups located at the basal plane and carboxylic acids groups at the structure edges" (Claramunt et al., 2015, mentioning Lerf et al., 1998). The control of oxygen functionalities attached to the carbo-layer is tuning the electronic and mechanical properties of GO, and therefore, GO "is often reduced by chemical agents, or thermal annealing, obtaining reduced graphene oxide (rGO)" (Claramunt et al., 2015, and references therein). For the reduction of GO, hydrazine or vitamin C are used. These agents introduce functional groups with amino nitrogen atoms when hydrazine is used or some O-groups with the reduction by means of vitamin C. "Alternatively, GO of different oxidation grade can be obtained by *thermal reduction*" (Claramunt et al., 2015, and reference therein).

According to Claramunt and coworkers, the chemical and thermal reductions are creating defects which alter "the physical and chemical properties of graphene-based materials. Then, taking into account the important role of defects in the properties of these materials, it becomes necessary to develop an *accurate methodology* to study them. Raman spectroscopy … has been widely used to study graphite and graphene" (Claramunt et al., mentioning Jorio et al., 2011). The researchers describe the spectra in the following manner. The Raman peaks in crystalline graphene are G (~1585 cm^{-1}) and 2D bands (~2700 cm^{-1}), that is first- and second-order Raman modes. The peaks change their width in the spectrum of GO. "These changes were attributed to high defect concentration related to the oxidation and are accompanied by the appearance of an intense peak centered at~1350 cm^{-1}, called the D band. The D band is related to the A_{1g} breathing mode, and it is observed because graphite oxidation and the subsequent reduction of GO seriously alter the basal plane structure of graphene" (Claramunt et al., 2015, and references therein). Other weak bands between 1100 and 1800 cm^{-1} can be observed in the spectra of GO as flakes and powders. These peaks are not present in pristine graphene or graphite. Some defects consist in "rings with different numbers of C atoms and configurations of C−O bonds. In these cases, a peak centered at~1620 cm^{-1}, D' band," is appearing (Claramunt et al., 2015, and references therein). Literature is also reporting a peak located between 1150 and 1200 cm^{-1} (D*) and a broad peak between 1500 and 1550 cm^{-1} (D'') (see the graphical abstract by Claramunt et al.). In soot and carbon black too, these peaks have been evidenced. Claramunt et al. provide an extensive and detailed discussion of literature about the origin of the peaks they mentioned.

Claramunt and coworkers are proposing several Raman spectra of GO and annealed GO. No significant differences are evidenced. "All the spectra present D and G peaks centered at~1350 cm^{-1} and~1585 cm^{-1} respectively, and the splitting of 2D Raman-active bands centered at ~2900 cm^{-1}. … an important feature is the presence of *a broad shoulder* between D and G peaks. The Raman spectral analysis of graphene derivatives often neglected this *shoulder* because it is very weak; nevertheless, it has been described in the Raman spectra of some carbon-based materials. Some authors fitted this shoulder using five functions which were ascribed to G, D, and D' bands and two poorly understood peaks, referred to as D*(~1150−1200 cm^{-1}) and D'' (~1500−1550 cm^{-1})" (Claramunt et al., and references therein). Claramunt and coworkers fitted the Raman spectra of GO and rGO with three pseudo-Voigt and two Gaussian functions. In their Figure 2b we can find an example for a Raman spectrum of rGO annealed at700°C. The sketch in our Figure 3 is showing this case. In the Figure 4a by Claramunt et al, we can find the dependence of the position of the D'' and D* bands with the oxygen content (and also in the graphical abstract of their work).

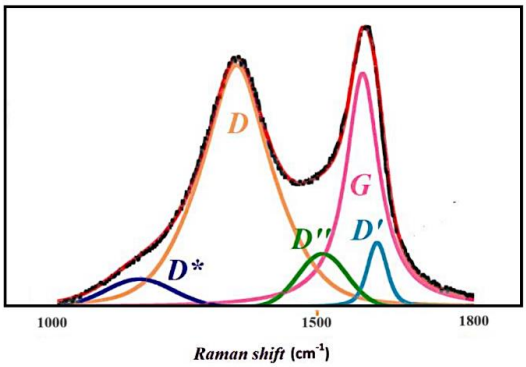

Fig. 3: A sketch of a Raman spectrum (first order part) in Claramunt et al., 2015, where we can find a notation of the peaks, different from that used by Beyssac et al., 2002, and Sadezky et al., 2005, where D is D1, D' is D2, D'' is D3 and D* is D4.

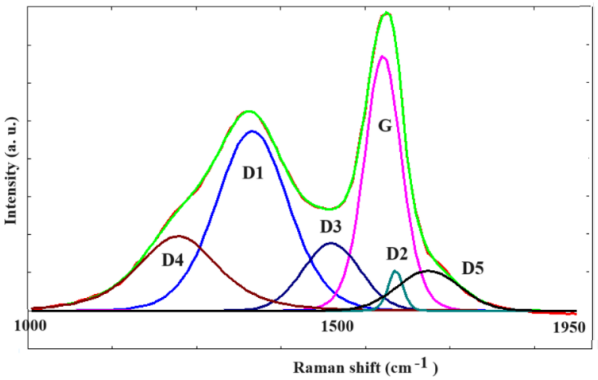

Fig. 4: Recovering the data (for biochar) from the Figure 2 by Sousa et al., 2020, we can propose a decomposition obtained by means of q-Gaussian Tsallis functions (see Appendix). From left to right, using Sousa et al. notation, the components are D4, D1, D3, G, D2 and D5. D5 is adjusting the fit (according to Sousa et al.).

For comparing the notations, in the Figure 4 we show the decomposition with q-Gaussian Tsallis functions (see Appendix) of the spectrum given by Sousa et al., 2020, in their Figure 2. In the shown decomposition, we used the q-Gaussians. These bell-shape functions are characterized by a shape parameter, the q-parameter, so that, when q is equal to 2 the curve is a Lorentzian curve. When q is close to 1, it is a Gaussian.

Graphene-based van der Waals (vdW) heterostructures

In Frisenda et al., 2020, graphite is mentioned among the naturally occurring van der Waals materials. It was "the exfoliation of two naturally occurring van der Waals minerals, graphite and molybdenite," that "shaped a whole new field of research", that of the 2D materials (Frisenda et al., 2020). In fact, in 2010, the Nobel Prize in Physics was awarded to Andre Geim and Konstantin Novoselov, for experiments regarding the two-dimensional graphene. The experiments concerned the exfoliation of graphite to obtain the single layers of graphene. Today, the "family of van der Waals materials that can be exfoliated to isolate 2D materials keeps growing" (Frisenda et al., 2020). Most materials are synthetic, but nature is providing plenty of van der Waals minerals that can have relevant applications. Therefore, it is fundamental to expand our investigation about Raman spectroscopy to van der Walls graphene-based heterostructures.

Let us consider Haidari et al., 2020, who studied the doping effect in graphene-graphene oxide interlayer. To study "the interlayer coupling effect in combined structures", Haidari and coworkers produced graphene and graphene oxide (GO) heterostructures. In particular, the researchers prepared graphene-, GO-, and graphene/GO areas on a SiO_2/Si substrate. The Raman spectra of these three regiones were then obtained. "As shown in Fig. 2a [in Haidari et al., 2020], the distinct Raman spectra for the three defined regions (graphene, GO, and graphene/GO) are clearly identified. For a CVD-fabricated monolayer graphene, the intensity ratio of 2D/G in the Raman spectra is determined to be approximately 3, which indicates that the graphene is crystalized".

The article by Haidari et al., 2020, is Open Access, under a Creative Commons Attribution 4.0 International License. Thanks to authors and Editor, we have the possibility to adapt the Figure 2 in Haidari et al., 2020, in our Figure 5.

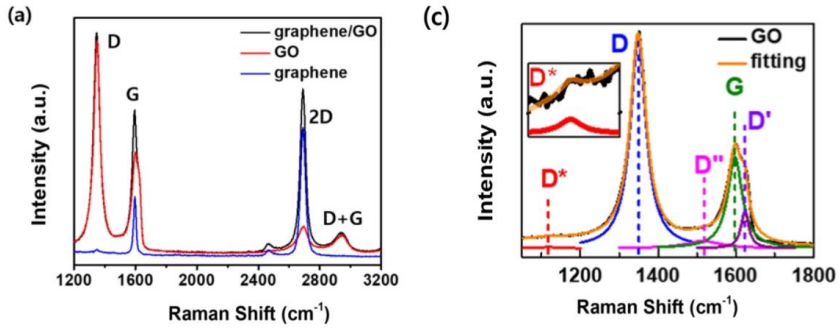

Fig. 5: Two panels of the Figure 2 in Haidari et al., 2020 (article and figures licensed under CC BY 4.0 DEED). The panel (a) is giving the Raman spectra, with evidenced the four peaks D, G, 2D, and D + G peaks, of graphene (blue), GO (red) and graphene/GO (black). For the D peak, the red and the black curves are almost coincident. Panel (c) is the Gaussian fitting results for the Raman spectrum of GO, with D (~1351 cm^{-1}), D' (~1623 cm^{-1}), D'' (~1515 cm^{-1}), G (~1597 cm^{-1}), and D* (~1120 cm^{-1}) peaks.

The simple building block

According to Li et al., 2023, "the fundamental mechanisms of Raman scattering of graphitic carbon materials have been revealed in detail thanks to the isolation and analysis of graphene, the simple building block of all graphitic carbon materials" (Li et al. are mentioning Novoselov et al., 2004, Ferrari et al., 2006, Geim and Novoselov, 2007). "Raman spectroscopy is particularly useful for the characterisation of graphene since its lack of a band gap means that all wavelengths of incident laser radiation are resonant" (Li et al. referring to Ferrari and Basko, 2013). This means that the Raman spectrum of graphene is massively resonantly enhanced enabling well-defined spectra to be obtained from graphene layers of only one atom in thickness" (referring to Ferrari et al., 2006). According to Li et al., the studies regarding graphene "have now solved many of the earlier unanswered questions for graphite and CNTs", carbon nanotubes. Li et al. are also concentrating on carbon fibers.

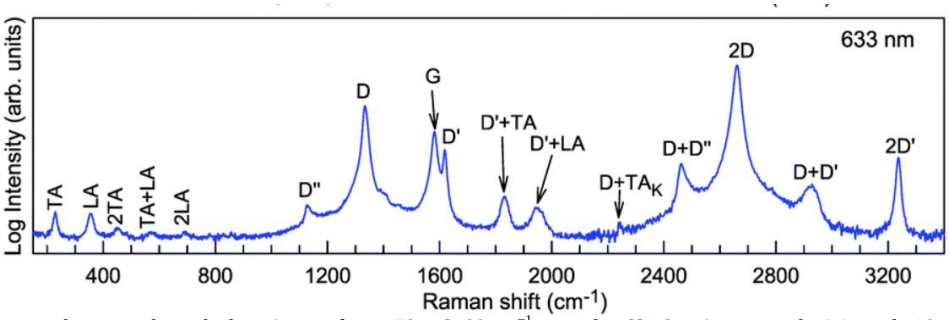

Fig. 6: The Raman modes in graphite whiskers (region from 150 to 3400 cm^{-1} excited at 632.8 nm), as given by Wu et al., 2018, Open Access, under CC BY-NC 3.0 DEED License. Data are by Tan et al., 2001. Note please the details of the spectrum enhanced using the semi-logarithmic scale.

Li and coworkers show in their Figure 3(a), the "number of Raman bands and their overtones [that] can be observed for carbon materials", referring to Wu et al., 2018, stressing that "care must therefore be exercised in the interpretation of Raman fingerprints of carbon materials as different structural features may give rise to a similar response". Let us consider Wu et al. and the Figure 3 of their article. The panel (a) in Li et al. is the panel (e) in Wu et al., which is giving "the expected Raman modes observed in graphite whiskers in the spectral region from 150 to 3400 cm^{-1} excited at 632.8 nm". The panel is told reproduced from Tan et al., 2001. Comparing the publications, it is evident that the figure 3(e) in the work by Wu et al. is an original layout, proposing data in a very detailed manner, and in semi-logarithmic scale (see our Figure 6). The article Wu et al., 2018, is Open Access, under CC BY-NC 3.0 DEED License. About graphite whiskers and other carbon-based materials, such as columnar carbons with a cone-shaped top, and needle- rods-like crystals, see Liu et al., 2023 Open Access.

From Wu et al., 2018, let us also propose their Figure 1, in the following Figure 7.

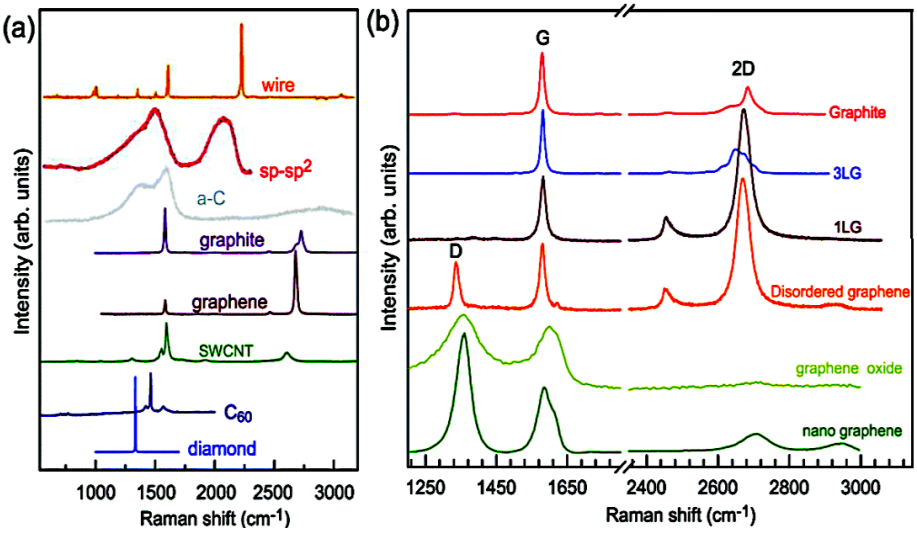

Fig. 7: The Figure 1 in Wu et al., 2018, CC BY-NC 3.0 DEED, is giving in the panel (a) the Raman spectra of "carbon solids and nanostructures, including 1D carbon wires, sp–sp^2 carbon, amorphous carbon (a-C), graphite, graphene, single-walled carbon nanotubes (SWNT), C60, and diamond. Raman spectra of carbon wire, sp–sp^2 carbon, a-C are reproduced with permission from" Milani et al., 2015, Open Access, CC BY 2.0 DEED, Copyright 2015, Beilstein-Institut. In the panel (b), we can see the Raman spectra of graphene-based materials, graphite, 1LG (monolayer graphene), 3LG, disordered graphene, graphene oxide and nanographene.

GO paper

Let us continue reading the article by Wu et al., 2018. "Under suitable conditions, [see references in Wu et al.] GO can undergo complete exfoliation in water, yielding colloidal suspensions of almost entirely individual graphene oxide sheets. Such sheets can be chemically functionalized, dispersed in polymer matrices, and deoxygenated to yield novel composites" (Wu et al., referring to Stankovich et al., 2006). Among the novel composites we can find the GO paper. "GO sheets can be assembled into a paper-like material under a directional flow. Vacuum filtration of colloidal dispersions of graphene oxide sheets yielded, after drying, free-standing GO papers with thicknesses ranging from 1 to 30 μm, as shown in Figure 31(a)" (Wu et al., referring to Dikin et al., 2007, and regarding the preparation and characterization of graphene oxide paper). In the panel (b), as evidenced by Dikin et al., we have well-packed layers through the cross-section of the GO paper. The Fig. 31(d) contains the Raman spectra of a typical GO paper. "The G peak and 2D peak are characteristic of sp^2 hybridized carbon–carbon bonds in graphene. The strong and broad D band and high I(D)/I(G) ratio in GO confirm its lattice distortions and a large amount of sp^3-like defects caused by the oxidation process" (Wu et al., 2018).

The article by Ejehi et al., 2020, Open Access, is proposing a use for the GO paper. In their research, a flexible graphene oxide (GO) paper was considered as the electrode for the Triboelectric Nanogenerators TENGs. "The all-flexible TENG has been employed as a self-powered humidity sensor to investigate the effect of raising humidity on the output voltage and current by applying mechanical agitation in two forms of using a tapping device and finger tapping". The article by Ejehi et al., 2020, is licensed under a Creative Commons Attribution 4.0 International License, http://creativecommons.org/licenses/by/4.0/. In our Figure 8, we reproduce the panels (c), (d) and (f) of the Figure 2 by Ejehi et al., 2020.

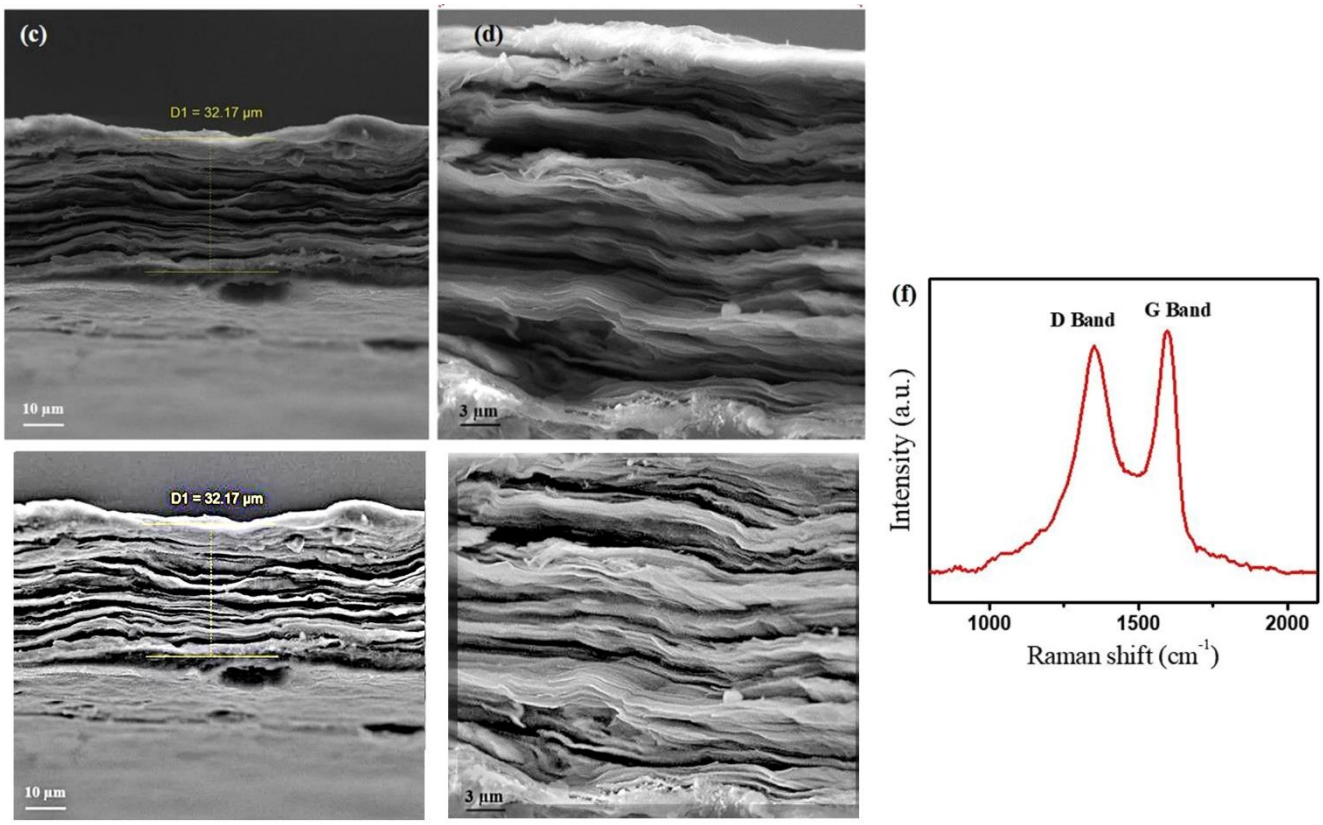

Fig. 8: In the upper part of the figure, we are showing the panels (c) and (d) in the Figure 2 by Ejehi et al., 2020, Open Access, CC BY 4.0 DEED. The panels show a cross-section SEM image. In the panel (f) a Raman spectrum is given. Below the original panel (c) and (d), we are proposing an enhancement of the SEM images obtained by means of the GIMP Retinex tool.

A remark

Before continuing the discussion about the Raman spectrum of graphene oxide, let us consider the article by Goldie et al., 2020. "Raman data are usually acquired by using Raman microscopy which couples a Raman spectrometer to an optical microscope, allowing high-magnification visualization of a sample and Raman analysis with a microscopic laser spot. In common with other microscale techniques a single spectrum *should not be used to characterize a macroscopic material.* While it is common for a representative Raman spectrum of a carbon sample to be reported, this is undesirable because of the variations likely to be present" (Goldie et al., 2020).

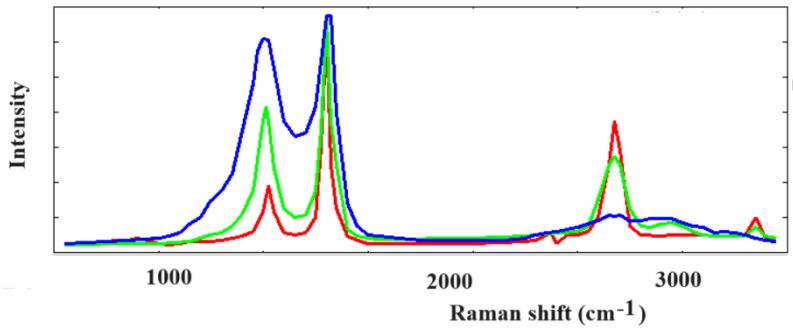

Fig.9: This sketch is representing what is given in the Fig.1a by Goldie et al., 2020. The three different spectra are coming from the same material.

Figure 1a, in Goldie et al., 2020, highlights what told by Goldie and coworkers, by means of three different Raman spectra from the same material. "Based on the evidence of only one spectrum, this material could be highly oxidized graphite or few-layer graphene, whereas in fact the sample is mostly graphitized carbon. One potential solution adopted by some is to collect multiple spectra from a sample and build a statistically meaningful picture of the material being analyzed" (Goldie et al., 2020). The spectra proposed in the Figure 1a by Goldie et al. are here given by the sketch in the Figure 9.

GO with different degrees of oxidation

In Sardinha et al., 2020, we can find the Raman spectra of GO with different degree of oxidation (see please the article for the detailed discussion of the preparation of GO). The researchers obtained five oxidation degrees with a synthesis which is using 2.0, 2.5, 3.0, 4.0, and 5.0 g of oxidizing agent for each 1.0 g of graphite. The authors are discussing the Raman spectroscopy of carbon-based materials, considering the features that we have already seen in the literature mentioned above. "The first order reveals the domain of two characteristic D and G bands." The D band (from 1350 to 1380 cm^{-1}) is giving a measure of the disorder in the crystalline structure. The G band, from 1575 to 1600 cm^{-1}, "is a characteristic of carbon-carbon vibration in the plane of the aromatic layers" (Sardinha et al., 2020).

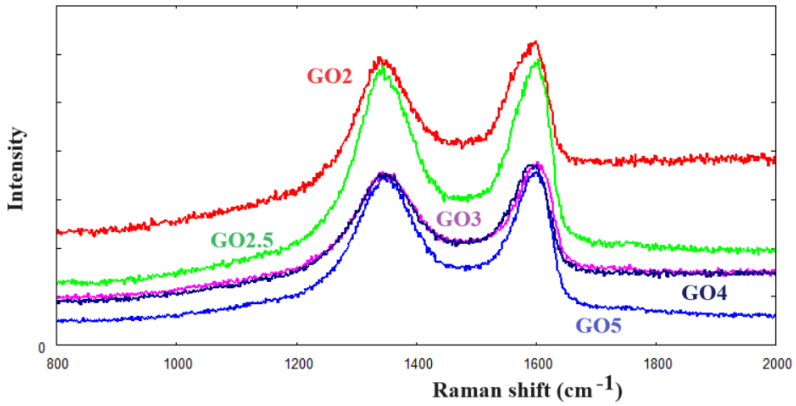

Fig.10: In Sardinha, 2019, Mendeley Data, CC BY 4 licensed, we can find the Raman spectra of GO with five different degrees of oxidation. The five oxidation degrees have been obtained with a synthesis using 2.0, 2.5, 3.0, 4.0, and 5.0 g of oxidizing agent for each 1.0 g of graphite. Here we show the first order part of the spectra.

The Fig.2 in Sardinha et al., 2020, is giving the spectra of graphite and GO with the five different oxidation degrees. The researchers conclude that the "GO spectra show G band with carbon domains with sp^2 hybridization and D band with carbon domains with sp^3 hybridization, which is also related to domains of O atoms. For second-order Raman spectra, [and Sardinha and coworkers mention Mishra and Ramaprabhu, 2012], four bands can be deconvoluted for GO spectrum with their respective peak positions of 2545 cm^{-1} (assigned to G*), 2690 cm^{-1} (assigned to 2D (G'')), 2925 cm^{-1} (assigned to D + D''), and 3160 cm^{-1} (assigned to 2D'')." (Sardinha et al., 2020). The comparison with graphite spectrum shows that "D band width increased as a function of the oxidation degree increase, which is associated with the increase of defects in the GO basal and edge planes." Moreover, Sardinha et al. mention the work by Ferrari and Robertson, that "attributed the [observed] G band displacement to the formation of new carbon atoms with sp^3 hybridization in the graphite network. They associated this displacement to the doping of the graphene layers or, in more oxidized samples, to the number of defects generated in the graphene sheets". Following the literature about fitting processes, Sardinha and coworkers "established a method to fit GO Raman spectra with different oxidation degrees taking into account the disorder influence on first and second-order band features. Thus, the fitting for the

first-order region was performed from 1000 to 1800 cm^{-1} using *five peaks* named as D*, D, D**, G, and D'' at around 1190, 1350, 1500, 1580, and 1610 cm^{-1}". The researchers use a notation different from that of Claramunt et al. and from that of Sadezky et al., 2005. For what is regarding the I_D/I_G ratio, as "indicator of disorder degree", Sardinha and coworkers used the *peaks areas* and G as G_{app}= G + D'', referring to King et al., 2016. A very interesting result is given for the A_D/A_{Gapp} behavior in Fig. 4 by Sardinha et al., 2020.

In King et al., 2016, it is remarked that "the peak commonly labelled G in the Raman spectra of GO and rGO samples is in fact a *superposition* of the G and D' peaks (the G_{app} peak) [in the Claramunt et al. notation]" (see examples in the Figure 2 by King et al.). The apparent G peak is named as "G_{app}". "This superposition renders the I_D/I_{Gapp} ratio an unreliable measure for the reduction of GO and has prevented it from accurately describing some of the recently reported GO and rGO samples. [King et al.] propose that the best measure of GO reduction is the difference in the positions of the D'_{inf} and G_{app} peaks, i.e. $D'_{inf} - G_{app}$" (King et al., 2016). The inferred D' mode is named as "D'_{inf}".

Interpretation (Ferrari and Robertson)

Sardinha and coworkers are referring, among many others, to the work by Ferrari and Robertson, 2000. Let us consider this article because of the interpretation we can find in it of D and G bands. As told by Ferrari and Robertson in their introduction, the "versatility of carbon materials" is due to their properties related to the ratio in them of sp^2-graphite-like to sp^3-diamond-like bonds. The sp^2-bonded carbons are producing a graphitic order, "ranging from *microcrystalline graphite to glassy carbon*". An amorphous carbon can be considered as a mixture of sp^3, sp^2, and also sp^1 sites, with the presence of hydrogen up to 60%, resulting in compositions as in the ternary phase diagram shown in the Fig. 1 given by Ferrari and Robertson. In this diagram we can find the diamond-like carbon (DLC) defined as the amorphous carbon "with a significant fraction of sp^3 bonds" (for other materials, see please the discussion in Ferrari and Robertson).

The work by Ferrari and Robertson is centered on Raman spectroscopy. Diamond has the T_{2g} 1332 cm^{-1} zone center mode, according to Knight and White, 1989. The disordered graphite has two sharp peaks, G around 1580–1600 cm^{-1} and D around 1350 cm^{-1}, "usually assigned to zone center phonons of E_{2g} symmetry and K-point phonons of A_{1g} symmetry, respectively". And here, we find a fundamental observation made by Ferrari and Robertson: "the unusual fact is that G and D peaks, of varying intensity, position, and width, continue to dominate the Raman spectra of nanocrystalline and amorphous carbons, even those without widespread graphitic ordering".

Discussing the Raman processes in disordered carbons, according to Ferrari and Robertson, "the visible Raman spectrum depends fundamentally on the ordering of sp^2 sites and only indirectly on the fraction of sp^3 sites". The researchers continue presenting a "three-stage model relating the visible Raman parameters to the sp^2 nanostructure and content of disordered carbons". The Section III of their work is dedicated to the vibrational modes, and in its Figure 3 we can find the vibrational density of states, VDOS, of graphite (in fact, of a single layer graphene) and of diamond. "Graphite has a higher VDOS band limit than diamond because the sp^2 sites have stronger, slightly shorter bonds than sp^3 sites". Then, the VDOS of DLC is discussed, such as the related consequences on Raman spectra.

In the Section IV, we can find the "Raman scattering in disordered carbon". First, the "Raman modes in *single crystals* obey the fundamental selection rule $\mathbf{q}\approx 0$, where **q** is the wave vector of the scattered phonon". However, on phonons we have sample boundary effects and grain boundaries, that is, finite-size domains, and therefore "the selection rule is relaxed to allow the participation of phonons near Γ, with $\Delta q \sim 2\pi/d$, where d is the dimension of the crystalline domain". According to Nemanich, Solin, and Martin, 1981, "the Raman scattering intensity of a finite crystal is given by" (Eq.6 in Ferrari and Robertson):

$$I(\omega) = \frac{n(\omega)+1}{\omega}\sum_{q,j} C\left(q,\omega_j(q)\right)|F(q)|^2 \frac{\Gamma/2\pi}{\left(\omega-\omega(q)\right)^2+\Gamma^2/4}$$

where we have a weighted sum over phonon wave vectors and branches, of Lorentzian broadened phonon lines. Function $C\left(q,\omega_j(q)\right)$ is the Raman coupling coefficient, whereas $F(q)$ is a phonon wave-vector "uncertainty". The boson occupation factor is $n(\omega)$. In this equation, as shown by Nemanich and coworkers, we can find the dynamical structure factor for Stokes scattering, in origin the Fourier transform of the correlation function of fluctuations in the polarizability. The Lorentzian broadening, with a lifetime Γ for phonons, is substituting the δ function in the dynamical structure factor. In amorphous materials the intensity is given by the Shuker-Gammon formula, 1970:

$$I(\omega) = \frac{n(\omega)+1}{\omega} C(\omega) G(\omega)$$

Function $G(\omega)$ is the VDOS of the disordered network. This equation works well for *a*-Si and *a*-Ge, "which are sp^3 bonded only, … The visible Raman spectra of disordered carbons are in marked contrast" (Ferrari and Robertson, and references therein). "In contrast, the Raman spectra of all disordered carbons are dominated by the relatively sharp G and D features of the sp^2 sites. This could be ascribed to the much greater cross-section of the π states. Nevertheless, the prevalence of G and D-like features, even in amorphous carbons with little graphitic ordering, requires explanation" (Ferrari and

Robertson, and references therein).
The G mode of graphite, E_{2g} symmetry, is a mode (see Fig.4 in Ferrari and Robertson) that "does not require the presence of sixfold rings, and so it occurs at all sp^2 sites, not only those in rings. It always lies in the range 1500–1630 cm^{-1}, as it does in aromatic and olefinic molecules" (Ferrari and Robertson, mentioning Lin-Vien et al., 1991). D peak, about 1355 cm^{-1}, is due to a breathing mode with A_{1g} symmetry, and the phonons which are involved are those close to the K zone boundary. "This mode is *forbidden in perfect graphite* and only becomes *active in the presence of disorder*. The D mode is dispersive; it varies with photon excitation energy, even when the G peak is not dispersive" (Ferrari and Robertson and references therein). Please, consider the further discussion in Ferrari and Robertson about the D band and their "quasi selection rule".

In Ferrari and Robertson, we find mentioned the work by Mapelli, 1998, Mapelli et al., 1999, who showed the main Raman features of aromatic oligomers as possessing the same symmetries, E_{2g} and A_{1g}, of graphite. "They also showed that the eigenvectors of these oligomers or clusters can be mapped onto those of graphite phonons along the direction GKM. In particular, … (see the discussion in Ferrari and Robertson) … this indicates that aromatic clusters can be considered as a part of a graphite superlattice, both electronically and vibrationally. This simultaneous mapping means that the behavior and dispersion of the D and G peaks in graphite also holds for aromatic oligomers and clusters in disordered carbon" (Ferrari and Robertson, 2000).

And here, let us show a remarkable Raman spectrum, that has been obtained by Gavilan et al., 2022, from the COSmIC pyrene-generated nanograins. COSmIC is the Cosmic Simulation Chamber facility at NASA Ames Research Center. Using Lorentzian and Gaussian components, Gavilan and coworkers determined six bands, and we can clearly see the G and the D (in particular, D1) bands.

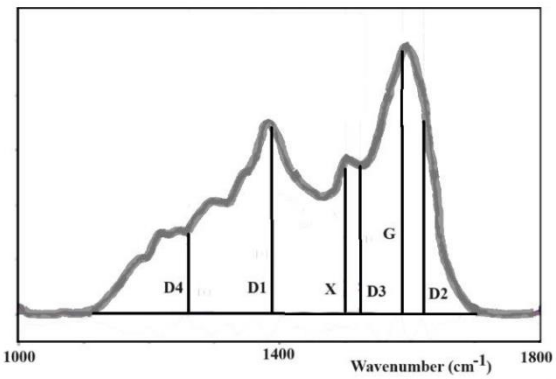

Fig.11: The grey line is giving the data obtained from COSmIC pyrene-generated nanograins, by Gavilan et al., 2022, in their Figure 5. Using Lorentzian and Gaussian components, Gavilan and coworkers determined six bands; the positions of their centers are here given by the black lines.

Let us return to Ferrari and Robertson, and to their point of view about the practical Raman spectroscopy.

"A practical point when *comparing different fitting parameters* for Raman spectra *is to know the fitting procedures used*. The Raman spectrum is a VDOS modified by a coupling coefficient, which incorporates various resonances. *There is no a priori reason to choose a particular function to fit the spectrum.* Empirically, the visible Raman spectra of amorphous carbons show one or two prominent features (the G and D peaks) and some minor modulations … The simplest fit consists of *two Lorentzians or two Gaussians*. A *Lorentzian fit is often used for crystals*, arising from *finite lifetime broadening*, and it is normally used for disordered graphite. A *Gaussian line shape* is expected for a *random distribution of phonon lifetimes in disordered materials*. A simple two symmetric-line fit is not always suitable, and one can find a multipeak fit" (Ferrari and Robertson, 2000).

"The most widely used alternative to a Gaussian fit is a Breit-Wigner-Fano (BWF) line for the G peak and a Lorentzian for the D peak". The BWF, which is asymmetric, can be reduced to a Lorentzian line shape for its specific feature parameter limit to 0. As observed by Ferrari and Robertson, the BWF curve has an increased power tail for lower frequencies. This allows the use of BWF lines to account for residual intensities, avoiding extra peaks. "The BWF+Lorentzian line pair is therefore an excellent means to fit Raman spectra of all carbons, from graphite to *ta*-C [tetrahedral amorphous carbon]. A Lorentzian line shape is used for the D peak as it is from the same family as the BWF line, while the various enhancement mechanisms for the D peak are consistent with a Lorentzian. However, any wide low-frequency tail of the BWF line will push the D peak to lower frequencies as the disorder increases. This significantly decreases the D peak size compared to a two-Gaussian fit. … . On one hand, smaller aromatic clusters have higher modes and shift D upwards. … Another important issue … [of the BWF lineshape], is that the maximum of the BWF line is not at ω_0 but lies at lower frequencies … [However,] the asymmetric BWF line shape is appropriate for the G peak due to the asymmetry of the VDOS of graphite or amorphous carbons towards lower wave numbers" (Ferrari and Robertson, 2000, and references therein).

Ferrari and Robertson add that "it is not always clear if the I(D)/I(G) ratio should be the ratio of the peak heights or peak areas. Generally, groups using BWF+Lorentzian fits report peak height ratios, while groups using two Gaussians report the area ratio. The difference is not so important for disordered graphite, as the peak widths are similar, but this is not so for amorphous carbons. In that case, - Ferrari and

Robertson explain - the broadening of the D peak is correlated to a distribution of clusters with different orders and dimensions, and thus the information about the less distorted aromatic rings is in the intensity maximum and not in the width, which depends on the disorder. Ring orders other that six tend to decrease the peak height and increase its width" (Ferrari and Robertson, 2000). I(D)/I(G) as the ratio of peak heights is mainly used by Ferrari and Robertson in their three-stage model, by means of which we can see how the position of the G peak changes and the D peak appears.

Besides the Gaussian, Lorentzian, and BWF functions mentioned above, Voigt, pseudo-Voigt and split-Lorentzian functions are used too. And we also have q-Gaussians and split-q-Gaussians for fitting Raman spectra.

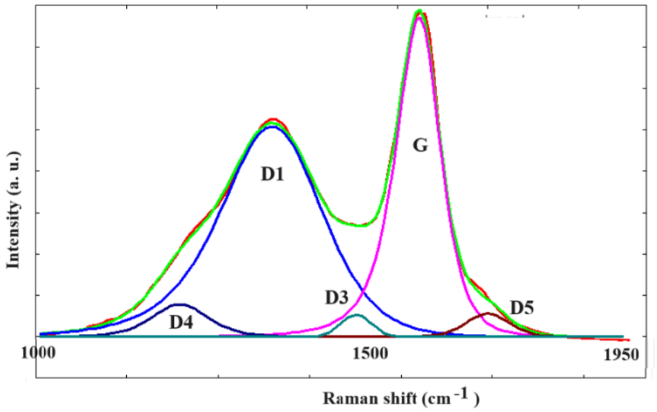

Fig. 12: As in the Figure 4, recovering the data (for biochar) from the Figure 2 by Sousa et al., 2020, we can propose a decomposition obtained by means of two split-q-Gaussian Tsallis functions for G and D1, and three q-Gaussians for D3, D4, and D5.

Lorentzian, Gaussian and q-Gaussian line shapes

Let us return to the graphene oxides. King et al. use Lorentzian lineshape. It seems that Sardinha et al. use Lorentzian and Gaussian functions as line shapes. In both cases, areas, and positions of the peaks of Raman spectra decompositions are depending on the considered line shapes. To show that the decomposition changes according to used functions, let us the consider the data from Sardinha, given in the Fig.10, and the Fityk software (Wojdyr, 2010). Fityk is a curve fitting and data analysis application, free and open source. It can perform a Levenberg-Marquardt algorithm, among other best fit algorithms. The function of merit is the weighted sum of squared residuals (WSSR), also called chi square. Fityk has several built-in functions but allows to execute a script with user-defined functions (see in the Appendix how we can define in Fityk q-Gaussian and split-q-Gaussian functions).

Let us consider the data of GO with degree 2, from Sardinha, 2019. The best fit with Lorentzian and Gaussian functions obtained by Fityk, is given in the Figure 13; the red dots are the data, the green curve the best fit, and the blue and magenta curves the components of decomposition.

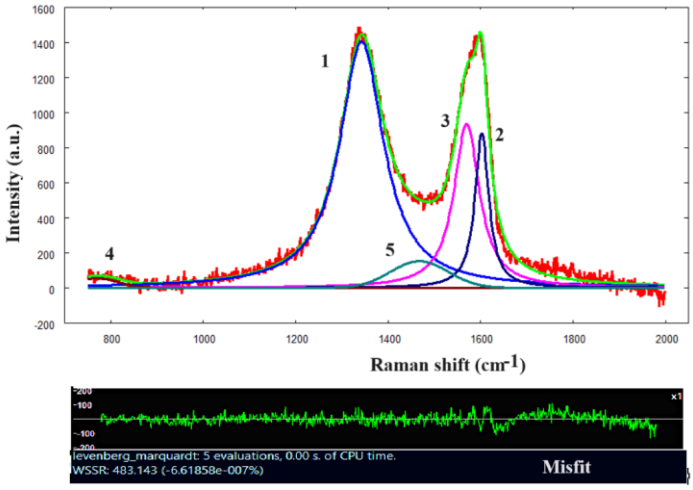

Fig.13: Curves 1,2 and 3 are Lorentzians, 4 and 5 Gaussians. Centers are 772 (5), 1343 (1, that is D1, D), 1469 (5, that is D3, D'' in Claramunt et al. notation), 1570 (3, G), and 1603 (2, D2, D'), in cm^{-1}. The lower part of the figure is giving the misfit. The sample GO2 data are a courtesy by Sardinha, 2019.

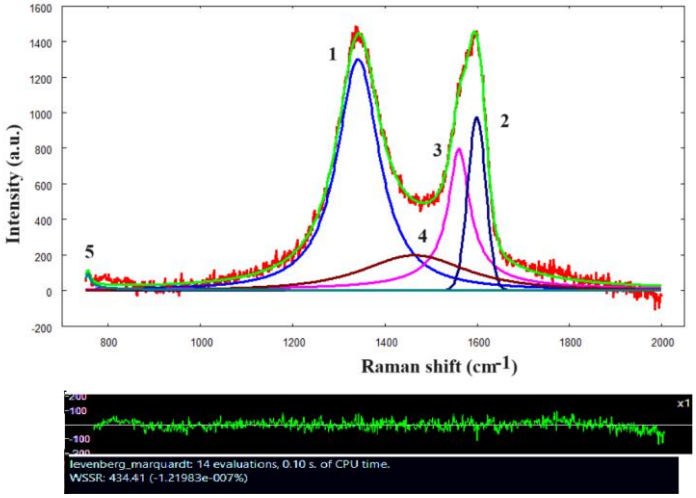

Fig.14: Curves 1-5 are q-Gaussians. Centers are 756 (5), 1342 (1, that is D1, D, q=1.89), 1465 (4, that isD3, D'' in Claramunt et al. notation, q=1.67), 1561 (3, G, q=2.43), and 1599 (2, D2, D', q=1.0), in cm^{-1}. The lower part of the figure is giving the misfit. The sample GO2 data are a courtesy by Sardinha, 2019.

In the Figure 14, a deconvolution with q-Gaussians is given. However, as suggested by Ferrari and Robertson about G peaks fitted BWF asymmetrically, we could use a split-q-Gaussian for G and a q-Gaussian for D. The result is shown in the following Figure 15.

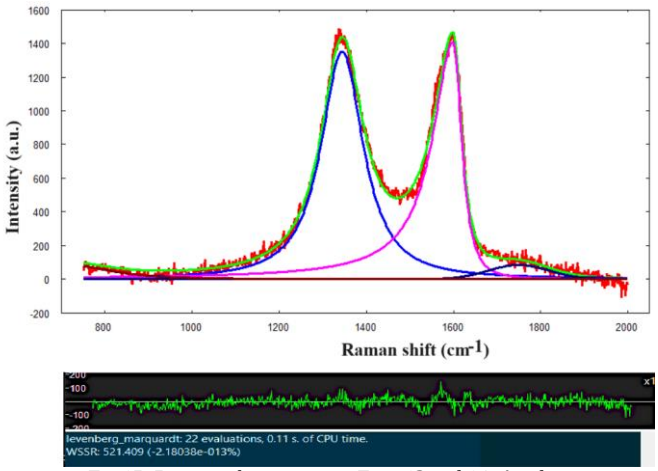

Fig.15: Data are the same as in Figs. 13 and 14. A split-q-Gaussians has been used for G peak, center 1599 cm^{-1}. For D, we used a q-Gaussian, q=1.88, center 1344 cm−1. Two further q-Gaussians have been used on the left and on the right. The sample GO2 data are a courtesy by Sardinha, 2019.

Let us pass to GO with degree 3, for instance. We can easily repeat what we did for GO with degree 2, as in the Fig. 13 and 14. However, we prefer to show the decomposition as in the Figure 15, with a slit-q-Gaussian for G, and q-Gaussian for D.

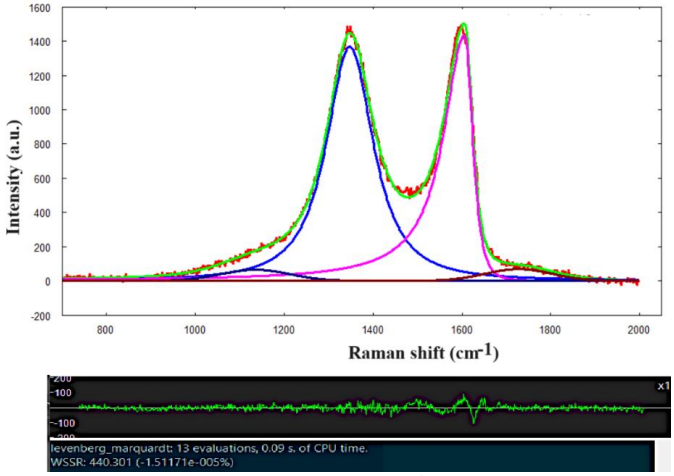

Fig.16: A split-q-Gaussians has been used for G peak, center 1605 cm−1. For D, we used a q-Gaussian, q=1.80, center 1347 cm−1. Two further q-Gaussians have been used on the left and on the right. The sample GO3 data are a courtesy by Sardinha, 2019.

As shown by the previous figures, the use of q-Gaussians instead of Lorentzian and Gaussian functions slightly changes positions and areas of the peaks. What is deserving further consideration is the use of asymmetric split-q-Gaussian functions. We can see from Fig.15 and 16, that we do not need the D3 component.

Discussion

The analysis of all the samples proposed by Sardinha et al. is beyond the aim of this review.

Ferrari and Robertson noted that, for comparing *different fitting parameters* of the Raman spectrum, it is fundamental the knowledge of *the used fitting procedures*. Once we have decided the number of components and their line shapes, we can compare the parameters obtained from a set of Raman measurements, such as those proposed by Sardinha et al., 2020. Since *there is no a priori reason to choose a particular function to fit the spectrum*, the use of q-Gaussians is good too. As shown by several analyses of Raman spectra with q-Gaussians (see Sparavigna, 2023, 2024), these functions can be efficiently used due to the power-law of their tails. The q-Gaussian tails have an intermediate behavior, between Lorentzian and Gaussian tails, and Gaussian and Lorentzian tails are rarely observed.

For what is regarding the role of the instrumental set-up, that is of its transfer function, this function had to be deconvoluted from the recorded spectra (Rautian, 1958, Seshadri and Jones, 1963, Merlen et al., 2017). The true spectral distribution, which is subjected to "distortions both in the optical and recording parts of the apparatus" (Rautian, 1958), is replaced by the observed measured distribution. This is a further reason to stress once more that there is no a priori reason to choose a particular function to fit the spectrum, especially if we have not determined the instrumental transfer function.

Fano-Raman in Graphene

To conclude the review about graphene Raman spectra, we need to mention the Fano resonance too. Ferrari and Robertson suggest the use of a BWF line shape for the G band in carbonaceous materials. In general, BWF is considered to take the size effect of grain boundaries into account. To the work by Nemanich, Solin, and Martin, 1981, that we have previously mentioned, let us also add those by Richter, Wang, and Ley, 1981, and Campbell and Fauchet, 1986, who produced a "phonon confinement model" (PCM), modifying the Richter et al. model. PCM is producing an asymmetric line shape. However, asymmetry of line shape is also an effect of the Fano resonance (see please Miroshnichenko et al, 2010). In fact, "in addition to quantum confinement effect, electron-phonon interaction or Fano interaction also results broadening and asymmetry in Raman line shape of semiconductors" (Yogi et al., 2016). Yogi and coworkers consider in their work the quantum confinement effect and Fano effect individually and jointly, to determine the features of Raman lines. In fact, what we find mentioned by Yogi and coworkers in the case of semiconductors had already been considered previously for graphene.

In 2014, Hasdeo et al., considered the "Breit-Wigner-Fano line shapes in Raman spectra of graphene". An asymmetric BWF Raman line appears in graphene due to the "excitation of electron-hole pairs in the vicinity of the Dirac cone". Asymmetry is therefore consequence of an "interference effect between the phonon spectra and the electron-hole pair excitation spectra" (Hasdeo et al., 2014). In 2013, Yoon et al.

worked on the "Fano resonances and their strong doping dependence", using Raman scattering of single-layer graphene (SLG). "As the Fermi level is varied by a back-gate bias, the Raman G band of SLG exhibits an asymmetric line shape … The observed Fano resonance can be interpreted as interferences between the phonon and excitonic many-body spectra in SLG" (Yoon et al., 2013). Fano resonances have been also observed "in infrared spectra of bilayer graphene (BLG) in the presence of an energy band gap generated by a perpendicular electric field, which can be interpreted as the inference between the phonon and a continuum spectrum of electronic transitions near the bandgap" (Yoon and coworkers, referring to Kuzmenko et al., 2009, and Tang et al., 2010). Since 2010, many works have been published about Fano resonances in graphene. This large literature requires a further specific review.

From carbon layers to carbon nanotubes

Previously, we have considered the Raman spectra of graphene and graphene oxide to understand the number of lines and the line shapes to be used for decomposing the spectra. Here, let us pass to review some literature about the Raman spectroscopy of carbon nanotubes, focusing especially on the line shapes. As shown by literature, the Raman spectra are able of giving information on the nature of nanotubes (metallic or semiconducting) and if they are single- or multi-walled structures. The Raman spectroscopy is able of investigating even a single nanotube. In particular, we will stress the role of curvature in breaking the symmetry of carbon layers, to produce the observed Raman bands. Consider please our Fig.7, left panel, and compare the cases of graphite, graphene and single-walled nanotube, SWNT. We have a band, the G band, which is at about the same Raman shift, but the SWNT case is showing two components. This is intriguing, since we know that the G band is originated by the graphite layer. In the single-walled nanotubes, a graphite layer is rolled up to form the tube. Consequently, in the Raman spectra we must have the signature of curvature and related broken symmetry and quantization. The result is band splitting.

Let us start reviewing the literature on nanotubes, highlighting the existence of a Breit-Wigner-Fano line. We have encountered the BWF line in a previous discussion about molybdenum disulfide MoS_2 Raman spectroscopy.

Lorentzian and Breit-Wigner-Fano line shapes (2005)

In Dresselhaus et al., 2005, we can find a review of the Raman scattering processes in carbon nanotubes. Besides the theoretical discussion, experimental results are also proposed. "In 2D graphite, the so-called G band around 1582 cm^{-1} is the only first-order Raman peak". In the single-walled nanotubes, this band is "*split into many features* around 1580 cm^{-1}". Besides this band, we have another strong first-order Raman mode, which is the radial breathing mode (RBM) (Dresselhaus et al., 2015). "The RBM is a *unique* phonon mode, appearing *only* in carbon nanotubes and its observation in the Raman spectrum provides direct evidence that a sample contains SWNTs. The RBM is a bond-stretching out-of-plane phonon mode for which all the carbon atoms move coherently in the *radial direction*, and whose frequency is about 100–500 cm^{-1}. The RBM frequency is inversely proportional to the tube diameter and is expressed as $\omega_{RBM}=C/d_t$" (Dresselhaus et al., 2005, mentioning Jorio et al., 2001). The constant is C=248 cm^{-1} nm in the case of isolated SWNTs on a substrate made of SiO_2. This relationship between diameter and angular frequency is due to "the mass of all the carbon atoms along the circumferential direction, [which is] proportional to the diameter" (Dresselhaus et al., 2005).

In the Table I by Dresselhaus et al., 2005, we can find the Raman bands (in cm^{-1}) in graphite and SWNTs. The dispersive modes are given for laser excitation E_L=2.41 eV.

Modes:	*iTA*	*LA*	*RBM*	*IFM⁻*	*oTO*	*IFM⁺*	*D*	*LO*	*BWF*	*G*	*and overtones*
	288	*453*	*248/d_t*	*750*	*860*	*960*	*1350*	*1450*	*1550*	*1582*	

Note the BWF (Breit-Wigner-Fano) mode at 1550 cm^{-1}, which is given as a "plasmon mode, only metallic carbons". Both in graphite and in SWNTs, we have the D-band at 1350 cm^{-1}, one of the dispersive modes in carbon materials (Dresselhaus et al., 2002, Tuinstra and Koenig, 1970, Dresselhaus and Eklund, 2000, Thomsen and Reich, 2000, Kürti et al., 2002). The D-band at 1350 cm^{-1} has a frequency which "changes by 53 cm^{-1} as a result of changing the laser energy E_L by 1eV" (Dresselhaus et al., 2005). The modes are usually fitted with Lorentzian line shapes (Dresselhaus et al., mentioning Cançado et al., 2002), but the BWF mode requires an asymmetric line shape, the BWF line shape. In the section 3.6, by Dresselhaus et al., 2005, we can find described the Breit–Wigner–Fano lineshape as follow.

"The G-band of *graphite intercalation compounds* (GICs), and the G^- band feature in the Raman spectra of *metallic SWNTs* do not have a symmetric line shape". According to Dresselhaus and coworkers, it "can be fitted to a so-called Breit–Wigner–Fano (BWF) lineshape", given in the form:

$$I(\omega) = I_0 \frac{[1 + (\omega - \omega_{BWF})/q\,\Gamma]}{1 + [(\omega - \omega_{BWF})/\Gamma]^2}$$

The parameters are described as: "1/q represents the asymmetry of the shape (interaction), while ω_{BWF}, I_0 and Γ are fitting parameters of the central frequency, the intensity, and the broadening factor, respectively. The BWF signal appears only when the electronic density of states at the Fermi energy has a finite value" (Dresselhaus et al., 2005). Dresselhaus et al., 2005, "observe a BWF lineshape only in *metallic* SWNTs, donor or accepter GICs, but not in semiconducting SWNTs or in graphite. The BWF spectral shape occurs when a *discrete* energy excitation level interacts with a *continuum* of energy excitations, causing a resonance and anti-resonance [Fano] effect (1/q), and thus giving rise to a non-symmetric spectral lineshape for the discrete state. … In the case of graphite and SWNTs, since the interaction with continuous states depends on the density of states at the Fermi energy, [Dresselhaus and coworkers] consider the origin of the continuum spectra to be a low-energy plasmon".

Note that, in Dresselhaus et al., 2005, the broadening of the band is ascribed to phonon-plasmon interaction. In Lazzeri et al., 2006, this point is questioned, and phonon-electron interaction assumed. Please, consider also that in the previous discussion about graphene we used the q-Gaussian functions. The q-parameter in the q-Gaussians is different from the q-parameter characterizing the Fano asymmetry.

The G-band in nanotubes is proposed in detail by Dresselhaus et al., 2005, as follows: "In contrast to the *graphite* Raman G band, which exhibits *one single Lorentzian peak* at 1582 cm^{-1} related to the *tangential* mode vibrations of the C atoms, the SWNT G-band is composed of *several peaks* due to the phonon wave vector confinement along the SWNT circumferential direction and due to *symmetry-breaking* effects associated with SWNT *curvature* [see Figs. 14(a) and 15 in Dresselhaus et al., 2005]". The measurement of the G-band frequency allows to characterize the nanotube diameter, and "to distinguish between metallic and semiconducting SWNTs, through strong differences in their Raman lineshapes [Dresselhaus and coworkers mentioning Jorio et al., 2003, Dresselhaus et al., 2003]". Moreover, the G band is sensitive to charge transfer due to doping SWNTs, besides being linked to "the selection rules in the various Raman scattering processes and scattering geometries."

In the Fig. 14(b) by Dresselhaus and coworkers we find the G-band for SWNTs made of two *main* components, G^+ at 1590 cm^{-1} and G^- at about 1570 cm^{-1}. "The G^+ feature is associated with carbon atom vibrations along the nanotube axis (LO phonon mode) and its frequency G^+ is sensitive to charge transfer from dopant additions to SWNTs", as it happens in graphite intercalation compounds (GICs) (Dresselhaus et al., 2005, mentioning Dresselhaus and Dresselhaus, 2002, Enoki et al., 2003). "The G^- feature, in contrast, is associated with vibrations of carbon atoms along the circumferential direction of the SWNT (TO phonon), and its lineshape is highly sensitive to whether the SWNT is metallic (Breit–Wigner–Fano lineshape) or semiconducting (Lorentzian lineshape), as shown in Fig. 14(a)" (see Dresselhaus et al., 2005, and references therein).

About the optical modes, LO or TO, in metallic and semiconducting nanotubes, Lazzeri et al., 2006, stress the electron-phonon coupling (EPC) as "the major source of broadening for the Raman G and G^- peaks in graphite and metallic SWNTs". The EPC is given as the responsible for G^+ and G^- splitting in *metallic* SWNTs. "This allows us to unambiguously assign the G^+ and G^- peaks to TO (tangential) and LO (axial) modes, *in contrast to what often done*" (Lazzeri et al., 2006, and references therein).

Returning to Dresselhaus et al., 2005, in their review we can find told that the Raman G band in the multi-wall carbon nanotubes, MWNTs, changes. "Because of the large diameter of the outer tubes for typical multi-wall carbon nanotubes (MWNTs) and because MWNTs contain an ensemble of carbon nanotubes with diameters ranging from small to very large, most of the characteristic differences that distinguish the Raman spectra in SWNTs from the spectra for graphite *are not so evident* in MWNTs. … the $G^+ - G^-$ splitting is large for small diameter SWNT tubes, the corresponding splitting of the G band in MWNTs is both small in intensity and smeared out due to the effect of the diameter distribution within the individual MWNTs, and because of the variation between different tubes in an ensemble of MWNTs in typical experimental samples. Therefore, *the G-band feature predominantly exhibits a weakly asymmetric characteristic lineshape, with a peak appearing close to the graphite frequency* of 1582 cm^{-1}" (Dresselhaus et al., 2005). That is, in MWNT we observe an asymmetric G band.

Curvature (2003)

In Jorio et al., 2003, it is stressed the role of curvature. "The Raman-allowed tangential mode in graphite", shifted at 1582 cm^{-1}, is the G mode (see figure 6 in Jorio et al.). "Unlike graphite, the tangential G mode in SWNTs gives rise to a *multi-peak feature*, also named the G band, where up to ***six*** *Raman peaks* can be observed in a first-order Raman process. However, a *simple analysis* can be carried out considering the ***two*** most intense peaks, that basically originate from the *symmetry breaking* of the tangential vibration when the graphene sheet is rolled to make a cylindrically shaped tube" (Jorio et al., 2003). The two main components of the G band are G^+, for mode displacements along the axis of the nanotube, and G^-, for mode displacement "along the circumferential direction". "The lowering of the frequency for the G^- mode is caused by the *curvature of the nanotube which softens the tangential*

vibration in the circumferential direction" (Jorio et al., 2003). Moreover, in metallic and semiconducting SWNTs, the G band is different in the shape of the G^- feature. In metallic SWNTs the G^- line is broader than that observed in semiconducting nanotubes; "this broadening is related to the presence of free electrons in nanotubes with metallic character" (Jorio et al., mentioning Pimenta et al., 1998, and Brown et al., 2001). "This broadened G^- feature is usually fit using a BWF line that accounts for the coupling of a discrete phonon with a continuum related to conduction electrons" (Jorio et al., mentioning Brown et al., Jiang et al., 2002). Also in Jorio et al., 2003, we find stressed that the "BWF line is observed in many graphite-like materials with metallic character, such as n-doped graphite intercalation compounds (GIC), n-doped fullerenes, as well as metallic SWNTs".

Plasmons (2002, 2005)

In Jiang et al, 2002, we can find a "strong enhancement of the Breit-Wigner-Fano Raman line in carbon *nanotube bundles* caused by plasmon band formation". The three main features in Raman spectra of nanotubes are the RBM, the mode of disordered carbon (D line) and the *G lines*, originated by the tangential vibrations of the carbon atoms. "For *metallic SWCNTs* an *additional band* close to the *doublet of G lines* (~1550 cm^{-1}) can be observed, which can be well fitted by a BWF line shape. This band results from coupling of phonons to the electronic continuum of the metallic tubes and is commonly used to distinguish between metallic and semiconducting SWCNTs. … It has been shown that the BWF band is *sensitive to the local environment* because the intensity is different in *chemically modified* tubes and tubes adsorbed on metal particles, i.e., in surface-enhanced resonance Raman scattering [SERS]" (Jiang et al., 2002). The Breit-Wigner-Fano line of individual SWCNTs and their bundles have been investigated, "finding that line intensity increases strongly with the bundle thickness" (Jiang et al., 2002).

In Paillet et al., 2005, however, we find the "vanishing of the Breit-Wigner-Fano component in individual single-wall carbon nanotubes". "In order to *decide definitely on* the dependence of the intensity of the BWF component with the size of the *bundle*, [Paillet and coworkers] have measured the radial breathing modes and tangential modes (TMs) of well-defined metallic individual single-wall carbon nanotubes (SWCNTs) and individual SWCNT bundles. In this aim, a complete procedure … has been developed. From this procedure, [Paillet and coworkers] show unambiguously that the BWF component vanishes in isolated metallic SWCNTs. In other words, the observation of a BWF component in the TM [tangential mode] bunch is an intrinsic feature of the metallic SWCNT *bundle*" (Paillet et al., 2005). Regarding the plasmons, see also Appendix.

Eigenvectors (2007)

In Thomsen and Reich, 2007, we can find described the "vibrational properties of single-walled carbon nanotubes", which are reflecting "the electron and phonon confinement as well as the cylindrical geometry of the tubes". "Metallic and semiconducting tubes can be distinguished from the high-energy Raman spectra. The high-energy phonons are remarkable because of their strong electron–phonon coupling, which leads to phonon anomalies in metallic tubes". Thomsen and Reich discuss the Raman-active phonons, and, besides their frequencies and symmetries, the electron–phonon coupling is also discussed in detail. Let us stress that in Thomsen and Reich we can also find the discussion of phonon eigenvectors. In fact, using "the point group and the positions of the carbon atoms the number and symmetry of the phonon eigenvectors" can be determined (see references in Thomsen and Reich). The symmetries of the eigenmodes are available by the Thomsen and Reich's Table 5. Let us note that, according to Thomsen and Reich, the "Raman spectrum of carbon nanotubes is dominated by scattering from totally symmetric phonons" (Thomsen and Reich, and references therein).

Let us consider the tangential modes as proposed by Thomsen and Reich.

"Tangential modes refer to all phonon bands of a nanotube originating from the *optical* phonons of graphite. Their eigenvectors are characterized by an *out-of-phase* displacement of two neighboring carbon atoms. The displacement is directed parallel to the nanotube wall, along the circumference, the axis, or a direction in between. … The Raman-active vibrations of the tangential modes fall into two groups, the high-energy modes (HEM) just below 1600 cm^{-1} and the D mode ≈ 1350 cm^{-1}. The HEM is also called the G line in the nanotube literature" (Thomsen and Reich, 2007).

"The *double-peak structure* close to 1600 cm^{-1} in Fig. 32b [by Thomsen and Reich] is a unique feature of single-walled carbon nanotubes" (the Figure is from J. Maultzsch, 2004). This feature "is a more reliable Raman signature of single-walled tubes than the RBMs in the low energy range. Typically, the most intense peak in the high-energy range occurs between 1592 cm^{-1} and 1596 cm^{-1} (depending on diameter and excitation energy); it is always higher in frequency than the corresponding peak in graphite (1589 cm^{-1}, and the smaller peak between 1560 cm^{-1} to 1590 cm^{-1} changes dramatically for resonant excitation of metallic tubes" (Thomsen and Reich, 2007).

In the Fig. 51 proposed by Thomsen and Reich, we can find the calculated line shapes of HEM in nanotubes. Kempa, 2002, made a theoretical work

about "the origin of the broad line below the highest mode in the Raman spectrum. He worked out the proposal by Brown et al., 2001, that the coupling of the tangential modes to the electronic continuum present in metallic nanotubes is the origin of the broad Raman line in the spectra. Semiconducting nanotubes, on the other hand, were responsible for uncoupled, Lorentzian-like peaks in the spectra". Therefore, Kempa assumed the plasmons in metallic tubes coupled to optical phonons. Due to the small wavevector of Raman excitation, a narrow peak is obtained. Therefore, Kempa added the presence of defects to have larger **q**-vectors in the phonon–plasmon scattering. "Alternatively, bundles of nanotubes form a plasmon continuum, similarly as electronic bands in a solid form from the discrete states of atoms. The calculated phonon–plasmon coupled lineshape for bundles is also shown in Fig. 51 and displays a broad Fano lineshape, more similar to experiment" (Thomsen and Reich, 2007). "An alternative explanation for the low frequency of one of the tangential modes in metallic nanotubes was put forward by Dubay et al., 2002. They found from first-principles calculations that in metallic tubes the Γ point frequency of the longitudinal optical phonon is softened by what is called a Peierls-like mechanism (it is a Kohn anomaly of the axial transversal branch)" (Thomson and Reich, 2007).

In Thomsen and Reich, we can also find a comparison of HEMs of bundled and isolated nanotubes by Telg et al., as given in the Figs. 52b and c of the review. "In Figs. 52b and 52c bundled tubes are compared to separated tubes at the same excitation energies. … The resonance of the metallic tubes is apparently much weaker in the isolated tubes compared to the bundled ones. The observations in Fig. 52 seem consistent with Kempa's [theoretical] suggestions, although the presence of a small Fano peak in separated tubes has remained controversial" (Thomsen and Reich are mentioning Paillet et al.).

In the Section 9 of Thomsen and Reich's work, we find discussed the Electron–Phonon Interaction. "The interaction between electrons and phonons is also one step in the Raman process and thus determines the scattering cross section or Raman intensity. … On the other hand, electron–phonon coupling can also affect the phonon frequencies and drive structural phase transitions in solids". Section 9 reviews the electron–phonon coupling in carbon nanotubes, then "the Kohn anomaly (also called Peierls-like phonon softening) in metallic tubes" is discussed.

TO and LO modes (2006)

After finding the plasmons mentioned in the article by Thomson and Reich, 2007, it is here strictly necessary to further consider the article by Lazzeri et al., 2006. Lazzeri and coworkers are discussing the "electron-phonon coupling in graphite and nanotubes". "The electron-phonon coupling (EPC) is a key physical parameter in nanotubes". In Lazzeri et al. letter, the researchers "prove that the optical phonons EPC are the major source of broadening for the Raman G and G^- peaks in graphite and metallic SWNTs. … The EPC are also responsible for the G^+ and G^- splitting in metallic SWNTs. This allows us to unambiguously assign the G^+ and G^- peaks to TO (tangential) and LO (axial) modes, in contrast to what often done" (Lazzeri et al., 2006, and the long list of references therein). Let us remember, from Dresselhaus et al., 2005: "the G^+ feature is associated with carbon atom vibrations along the nanotube axis (LO phonon mode) and … The G^- feature, in contrast, is associated with vibrations of carbon atoms along the circumferential direction of the SWNT (TO phonon)". Lazzeri and coworkers "dismiss the common assignment of the G^- peak in metallic SWNTs to a Fano resonance between phonons and plasmons" (Lazzeri et al. and references therein).

"Conflicting reports exist on the presence and relative intensity of the G^- band in isolated versus bundled metallic tubes. It has been claimed that this peak is as intense in isolated SWNTs as in bundles; that it is smaller; or that it can be absent. The G^- peak is also thought to represent a Fano resonance due to phonon coupling with plasmons" (see in Lazzeri et al. the detailed further discussion and references therein). Lazzeri and coworkers "show that, like in graphite, the EPC *per se* gives the main contribution to the G^- position and FWHM (Full Width at Half Maximum), even in the absence of phonon-plasmon coupling. Surprisingly, this has not been considered so far [2006]. However, it is clear that, if phonons do not couple to electrons, they certainly cannot couple to plasmons" (Lazzeri et al., 2006).

In Lazzeri et al., we find told that "in a metallic SWNT, the phonon frequencies corresponding to the graphene E_{2g} mode are affected by a Kohn anomaly". "The strength of the Kohn anomaly also depends critically on the quantization of the electronic wave functions along the nanotube circumference confinement effects. On the contrary, the curvature of the nanotube has a small effect on the strength of the Kohn anomaly. In fact, the curvature can affect the Kohn anomaly by modifying the strength of the EPC and the band dispersion for the states near the Fermi energy" (Lazzeri et al., 2006).

"The electron-phonon interaction is, besides the Coulomb interaction, one of the fundamental interactions of quasiparticles in solids. It plays an important role for a variety of physical phenomena. In particular in metals, low-energy electronic excitations are strongly modified by the coupling to lattice vibrations, which influences, e.g., their transport and thermodynamic properties. Electron-phonon coupling (EPC) also provides in a fundamental way an attractive electron-electron

interaction, which is always present and, in many metals, is the origin of the electron pairing underlying the macroscopic quantum phenomenon of superconductivity" (Heid, 2017).

G^- and G^+ in the Raman spectrum (2008)

Telg et al., 2008, studied the G^+ and G^- modes in a pair of a metallic and a semiconducting nanotube. "The G^- peak is the longitudinal mode of the metallic tube; it is broadened and downshifted due to strong electron-phonon coupling in the metallic nanotube. The G^+ peak is due to the longitudinal mode in the semiconducting tube. An asymmetric lineshape of the G^- peak agrees with observations of the asymmetry to be an intrinsic feature of metallic nanotubes". This is what we can find told by the abstract of Telg et al., 2008. It is therefore necessary to consider the article in more detail.

The HEM G^- and G^+ modes "are the most utilized features of carbon nanotubes to distinguish between metallic and semiconducting nanotubes" (Telg and coworkers, mentioning Krupke et al., 2003, Strano et al., 2003, Zheng et al., 2003). In an ensemble of nanotubes, with different chirality, we can always find a sharp G^+ peak about 1590 cm^{-1}, whereas "the lineshape and position of the G^- peak vary with excitation energy" (Telg et al.). In semiconducting nanotubes, in resonance G^- is similar to G^+; "when metallic tubes are coming into resonance the intensity of G^- increases, the peak shifts to lower energies, becomes broader and symmetric". The origin of the peaks in metallic nanotubes and the symmetric lineshape, in 2008, was still under debate and therefore, in Telg et al., we find the literature we have previously reported. "Initially the origin of metallic lineshape of the HEM was assumed to be electron-plasmon coupling in metallic nanotubes. It was suggested that in a bundle of metallic nanotubes, a continuum of plasmon states coupled to the TO phonon gives rise to the Fano lineshape, … broadened, downshifted and asymmetric. Referring to this model the lineshape in an isolated nanotube should be similar to the spectrum of a semi-conducting nanotube, since the continuum of plasmons is solely present in nanotube bundles. Another model predicts a strong electron-phonon coupling in metallic nanotubes. As a result, the LO-phonon is drastically downshifted below the frequency of the TO-phonon. Additionally this predicts a broad peak which is asymmetric due to the phonon coupling to the continuum of electrons close to the Fermi-level. In contrast to the model of an electron-plasmon coupling these effects should be visible in a bundle of metallic nanotubes as well as an isolated metallic nanotube" (Telg et al., 2008, and references therein).

In the article by Telg and coworkers we find the Raman measurements on the bundle of one metallic and one semiconducting nanotube. "Correlating the resonance conditions of the RBMs and the high-energy modes, G^+ and G^-, [Telg and coworkers] show that the G^- peak originates from the metallic and the G^+ peak from the semiconducting tube". An asymmetric G^- lineshape is observed, supporting "the idea that the Fano lineshape is an intrinsic property of metallic nanotubes". Moreover, the "observed G^+ and G^- peaks originate from LO-phonons in semiconducting and metallic nanotubes, respectively".

In the Figure 1 by Telg and coworkers, we can see the Raman spectrum of the bundle, with a laser energy of 2.04 eV. The presence of two radial breathing modes is indicating that the system is made of two nanotubes. Using several different excitation energies, the researchers found that G^- and G^+ peaks are due to different resonance conditions. "Therefore, the origin of the G^- peak is a different nanotube than the tube related to the G^+ peak. This is in contrast to the common assumption for such lineshape where both peaks are attributed to metallic nanotubes" (Telg et al., 2008).

Let us consider the HEMs in the Figure 1 by Telg and coworkers. Let us extract some data from the figure and start fitting to a BWF line and a Lorentzian line. Software Fityk (Wojdyr, 2010) is used (see in the Appendix how we can define the BWF in Fityk, and also q-BWF functions).

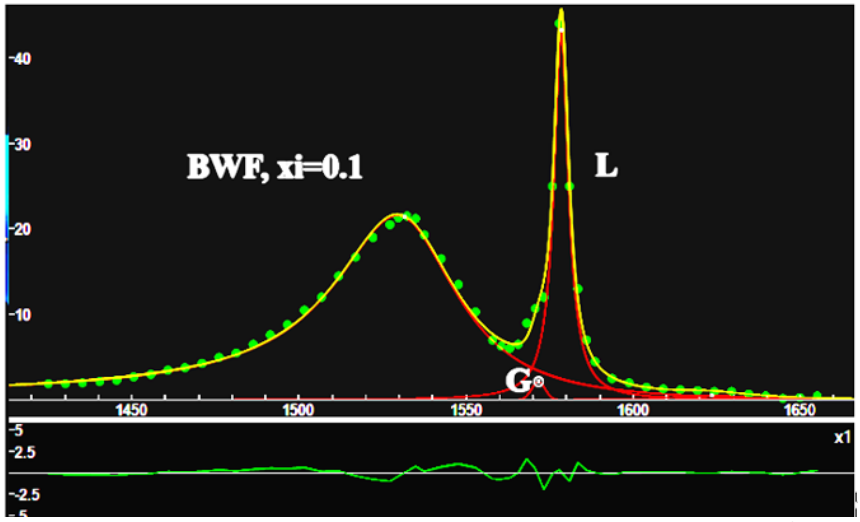

Fig.17: In this fit we consider the HEMs in the Figure 1 by Telg and coworkers, 2008. We extracted some points from that figure. The data are represented by green dots. The main modes are fitted to a BWF line and a Lorentzian line. The components are given in red, the sum of the component in yellow. The asymmetry parameter 1/q that we usually find in the definition of the BWF function is here substituted by $-\xi$ (see Appendix). A small Gaussian is added to describe what seems being a shoulder of the Lorentzian peak. An even smaller Gaussian has been used in the high-frequency tail. The lower panel of the image is giving the misfit.

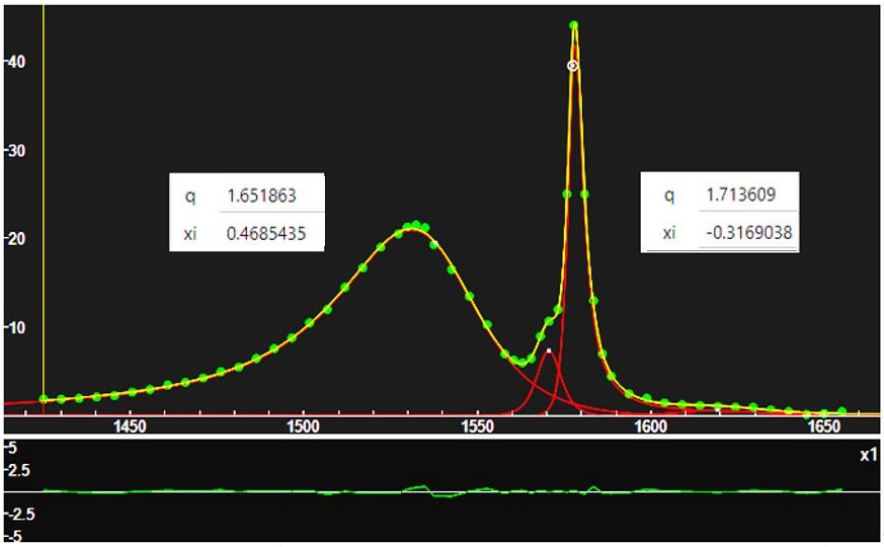

Fig.18: As in the Figure 3, here we use HEM data from the Figure 1 by Telg and coworkers, 2008. The modes are fitted to q-BWF lines (see Appendix). The q-parameter is a parameter characterizing a generalization of the exponential function in the framework of the Costantino Tsallis statistics. Therefore, the parameter 1/q that we usually find in the definition of the BWF function is here substituted by $-\xi$. A small q-Gaussian is added to describe the shoulder of the G^+ peak. An even smaller q-Gaussian has been used in the high-frequency tail. The parameters q and ξ are given close to the respective q-BWF peaks.

In the Figure 17, we fitted data to BWF and Lorentzian functions. A shoulder to this last peak was added to improve the fit. In the Figure 18, we used two q-BWF functions. Note the lower misfit. Both peaks seem being asymmetric, and they are not Lorentzians, but essentially q-Gaussians (intermediate functions between Gaussian and Lorentzian functions) in their shape (see Appendix).

A BWF line and two Lorentzian lines (2013)

Masaru Tachibana, 2013, proposed the "characterization of laser-induced defects and modification in carbon nanotubes by Raman spectroscopy" (open access, distributed under the terms of the Creative Commons Attribution 3.0 License). "The G band in SWCNTs is a more complex spectral feature. Due to the folding of graphene sheet into the SWCNT and the symmetry breaking effects associated with the nanotube curvature, G band splits into G^+ and G^-, which are related to atomic vibrations preferentially along (LO) and perpendicular (TO) to the tube (folding) axis, respectively, for semiconducting SWCNT" (Tachibana, 2013). "Perpendicular" TO means tangential optical mode.

"For metallic tubes, electron-phonon coupling softens the LO modes, so that G^+ and G^- are actually with TO and LO modes, respectively. The G^- peak for metallic tubes is fitted by asymmetric and broad BWF. … Actually, due to the symmetry breaking effects associated with the nanotube curvature, G band in SWCNT generates up to *six Raman-allowed* G-band peaks corresponding to two totally

symmetric A_1 modes, two E_1 modes and two E_2 symmetry modes. Three of each exhibit LO or TO-like vibration. Due to the delocalization effect and special resonance conditions, the A_1 modes usually dominate the G-band spectra" (Tachibana, 2013).

Examples of spectral decomposition are given in the Figure 5 of the article by Tachibana, where we can find the D and G Raman bands for pristine SWNTs, laser-irradiated SWNTs and annealed SWNTs after the irradiation. The G band has been fitted to two Lorentzian lines and one BWF line. The figure is from Kang et al., 2008. In Uchida et al., 2004, which is proposing the "temperature dependence of the Breit–Wigner–Fano Raman line in single-wall carbon nanotube bundles", we can find further examples of fitting to BWF components. "According to a previous report [Uchida et al., mentioning Brown et al., 2001], four Lorentzian lines located at 1542, 1561, 1592 and 1602 cm^{-1} can be assigned … [to the] modes in the G band of semiconducting SWNTs, while the Lorentzian and BWF lines, respectively, located at 1583 and 1541 cm^{-1}, can be assigned to be predominantly the A(A_{1g}) mode in the G band of metallic SWNTs" (Uchida et al., 2004). In fact, in the Fig.1 by Uchida et al., we can find a G band decomposed *in six components*. The largest component is the BWF. Then, we find five Lorentzian lines.

EPC (2021)

Jorio and Saito, in 2021, are giving a review (open access) about Raman spectroscopy for carbon nanotube applications. "For the specific case of single-wall carbon nanotubes (SWNTs) and also other graphene-related materials, RS [Raman Spectroscopy] has an extra aspect that makes it even more powerful, which is the highly efficient and selective resonance effects. The resonance effect makes it possible to measure one isolated carbon nanotube by RS and makes it possible to obtain information from the vibrational properties that are usually Raman inactive. Accessing phonons that are Raman inactive (e.g., phonons in the interior of the Brillouin zone) is important to characterize several static and dynamic properties" (Jorio and Saito, and references therein). Differently from the RBM, which is a feature of SWNT only, the G and G' (or 2D) bands are observed in all carbon structures. "What makes these features special for applications is twofold": 1) the high frequencies of the bands due to the small mass of the carbon atoms and 2) metallic structures exhibiting "a strong electron–phonon coupling for a phonon, enabling detailed sensing of the Fermi level position via Raman spectroscopy". The two effects are described by Jorio and Saito.

In Fig. 7(a), Jorio and Saito "show the G-band spectra for graphite (HOPG, top), semiconducting (middle), and metallic (bottom) SWNTs. Although the C–C bond stretching in graphene or graphite exhibits a single Lorentzian peak, SWNTs have two split peaks. This happens because in the flat hexagonal lattice of graphite, the three C–C bond stretching vibration for a carbon atom is isotropic. However, when you impose a curvature in the sp^2 network to form a nanotube, symmetry breaking occurs by a curvature-induced strain in the direction perpendicular to the tube axis, which lowers the phonon frequency of the C–C vibrations which are preferentially in the circumferential direction. On the other hand, the C–C vibrations in the direction parallel to the nanotube axis do not show the frequency shift" (Jorio and Saito, 2021). Consequently, a frequency splitting is induced by the curvature of the layer.

"In the case of semiconductor SWNTs, ω^+_G and ω^-_G correspond, respectively, to C–C bond stretching in the direction parallel (LO) and perpendicular (iTO) to the nanotube axis, when we consider the phonon propagating direction in the nanotube axis. However, in the case of metallic SWNTs, the assignment of ω^+_G and ω^-_G becomes opposite [(iTO) and (LO)] to that for semiconductor nanotubes. This inversion happens because the LO mode becomes soft by the Kohn anomaly effect" (Jorio and Saito, 2021), due to electron-phonon coupling. "This electron–phonon coupling can be tuned by doping a gate electrode on a device, and the phonon-softening phenomenon of the G band is an evidence for metallic SWNT, … Therefore, the analysis of the G-band line shape of metallic SWNTs, … can be used to monitor the Fermi level". See please also the Figure 9 in Jorio and Saito, which is showing how the spectrum changes when the investigated location in the sample is changed.

Multi-walled carbon nanotubes

In Heise et al., 2009, we can find the Raman spectra of multi-walled nanotubes, besides other carbon materials, such as the graphitised porous carbon (Carbotrap) and graphite, recorded with excitation wavelengths at 532 and 785 nm, "and analysed for band positions and shape with special emphasis paid to the D, G and G' bands. … Spectral features similar to those of the MWCNT filter varieties were observed for the Carbotrap material" (Heise et al., 2009). The spectra are shown by Heise and coworkers, in their Fig. 3(a) and (b) in the region 1200-2800 cm^{-1}. Specifically, the analyzed materials were SWCNTs Aldrich, two MWCNT filter varieties, MWCNT Aldrich, Carbotrap and graphite. "A rigorous line shape analysis of the Raman line profiles corresponding to G-band … was performed taking widely varying initial guesses for *three peaks*. However, each start value finally yielded the same wavenumber positions for the *three band components*. During the fitting of the measured Raman line profile, each component band was assumed to be a mixture of a Lorentzian and a Gaussian profile. … Although the fitting is done by taking the sum of Lorentzian

and Gaussian line shapes, a judicious mixture of the two profiles is nearly as good as a Voigt profile" (Heise et al., 2009). However, Heise and coworkers report that "Athalin and Lefrant, 2005, stated that only a single peak with a full width at half maximum (FWHM) larger 70 cm^{-1} would appear for MWCNT in contrast to the case of SWCNTs" (Heise et al., 2009).

"Besides the first-order D-band, the spectra of [Heise and coworkers'] graphite bar sample also show *another first-order band* at ~1620 cm^{-1}, which is called D2-band and accounts for the structural disorders. Like the G-band of graphite, the D2-band also corresponds to a graphitic lattice mode with E_{2g} symmetry" Heise et al., mentioning Sadezky et al., 2005)

Heise and coworkers stress that multiple splitting of the G-band modes is observed "for individual MWCNTs by Zhao et al., 2002, who stated that for verifying the symmetry assignments, polarised Raman scattering studies would be needed". Further references to studies about polarized Raman spectroscopy of aligned MWCNTs and about the influence of the diameters in the Raman spectra of multiwalled aligned CNTs are Rao et al., 2000, and Antunes, et al., 2007. Let us stress that Heise and coworkers observed in the Raman spectra of Carbotrap "a spectral feature similar to that of CNTs".

Examples

Di Tinno et al., 2022. In their article we can find Raman spectra of MWNTs and SWNTs, purchased from Heji Inc. (Hong Kong) and Nanointegris Technology Inc. (Boisbriand, QC, Canada), respectively. This article is an open access article distributed under the terms and conditions of the Creative Commons Attribution (CC BY) license (https://creativecommons.org/licenses/by/4.0/).

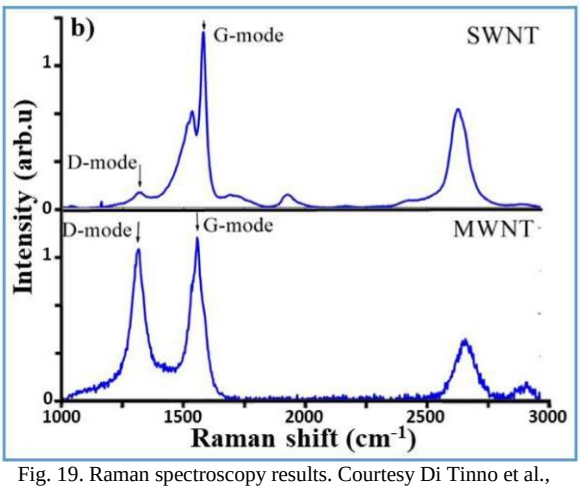

Fig. 19. Raman spectroscopy results. Courtesy Di Tinno et al., under CC BY 4.0 license.

Bokobza et al., 2015. In their article we can find the following Raman spectrum of MWCNTs. This article is an open access, CC BY 4.0 license (https://creativecommons.org/licenses/by/4.0/).

Figure 1 by Bokobza et al. "compares the Raman spectra of the different carbonaceous materials excited at 633 nm. These spectra show deconvolutions into Gauss–Lorentz band shapes after a hand-made subtraction of the baseline". No information is given about MWCNTs material. The researchers say that the decompositions are made by means of Gauss-Lorentz functions.

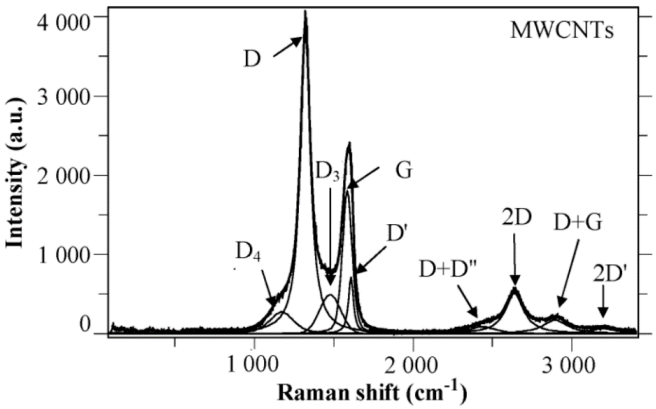

Fig.20. Raman spectroscopy results. Adapted from courtesy Bokobza et al., under CC BY 4.0 license. For the notation, see discussion in chemRxiv.

The D' (D2) band

Discussing graphene and graphene oxide Raman spectra we have seen the presence of a D' band (also known as D2 band). In the figure by Bokobza et al., the D' band is evidenced by the decomposition of the spectra, obtained by means of "Gauss-Lorentz band shape". It seems they used a pseudo-Voigt line shapes, that is linear combinations of Gaussian and Lorentzian functions. About the D' component, let us consider Osswald et al., 2007. "Unlike SWCNTs and DWCNTs, MWCNTs show an additional Raman band at about 1615 cm^{-1} called the D' band. This band is a Raman feature induced by disorder, defects or ion intercalation between the graphitic walls" (Osswald et al., 2007).

Osswald and coworkers monitored oxidation of MWCNTs by Raman spectroscopy. "CNTs usually tend to agglomerate in bundles or other aggregates … To improve their solubility, CNTs have been functionalized by different methods. The easiest way to covalently attach chemical groups … is by oxidation". Moreover, it is noted that "MWCNTs originally have two areas with different reactive sites: the fullerene-like tube-ends and the less reactive hexagonal cylindrical tube walls. Carbon bonds at the tips are under higher strain due to their larger curvature and provide an area of enhanced reactivity and lower activation energy for the oxidation reactions. … local defects in the walls of the nanotube lead to a similar reduction in the activation energy and lower oxidation temperatures" (Osswald et al., 2007). In the Raman spectra given in the article,

the presence of D' peaks is evident.

Discussion

The G band has a large variety of line shapes. In general, in the case of SWNTs, we can find several components, usually fitted to Lorentzian line shapes. In the case of metallic nanotubes, the presence of a BWF line shape is also invoked. In Ferrari and Robertson, 2000, we find told the BWF line shape as suitable to represent, in general, the G band of carbonaceous materials. For MWNTs, the G band is also accompanied by a D' shoulder. Lorentzian and pseudo-Voigt lines are used. We have therefore the possibility of using different line shapes.

Ferrari and Robertson made an important observation about the BWF line, that it is an efficient way to fit the data. In fact, both symmetric and asymmetric bands can be fitted to BWF lines. However, we have deviations from the Lorentzian line shape too, and in fact, Voigt and pseudo-Voigt line shapes are often preferred. In 2023, we proposed for Raman spectroscopy a generalization of the Lorentzian profile as a q-Gaussian line shape. As shown on many occasions, the q-Gaussian is suitable for fitting Raman spectra (from those given in SSRN to the SERS cases, and others). It means that we can consider a Lorentzian line shape and deform it by means of the q-Gaussian. Consequently, let us use a q-BWF line shape to deform the BWF, so that we can contemplate, in one line shape, symmetry and asymmetry, Lorentzian and Gaussian features. To deform BWF, let us define q-BWF function as follows:

$$BWF = C\frac{\left[1-\xi\gamma^{1/2}(x-x_o)\right]^2}{\left[1+\gamma(x-x_o)^2\right]}$$

When parameter ξ is zero, BWF becomes a Lorentzian function. Therefore, it is easy to turn BWF into a q-BWF function:

$$\text{q-BWF} = C\left[1-\xi\gamma^{1/2}(q-1)^{1/2}(x-x_o)\right]^2\left[1+(q-1)\gamma(x-x_o)^2\right]^{1/(1-q)}$$

Please consider that in literature about Fano resonance (or Fano interference) the asymmetry parameter ξ is often given by 1/q (and with an opposite sign). Here the q-parameter is related to the Tsallis statistics. The parameters in the q-BWF, ξ and q, can be used to estimate the asymmetry and the deviation from the Lorentzian shape respectively.

As an example, let us consider the highly oriented pyrolytic graphite Raman spectrum data from the supporting information for "Graphene fabrication via carbon segregation through transition metal films", 2017, kindly made available by D. Pudikov. Let us use q-BWFs for all the components of the spectrum. In the following two figures, the details of the G and 2D bands are given.

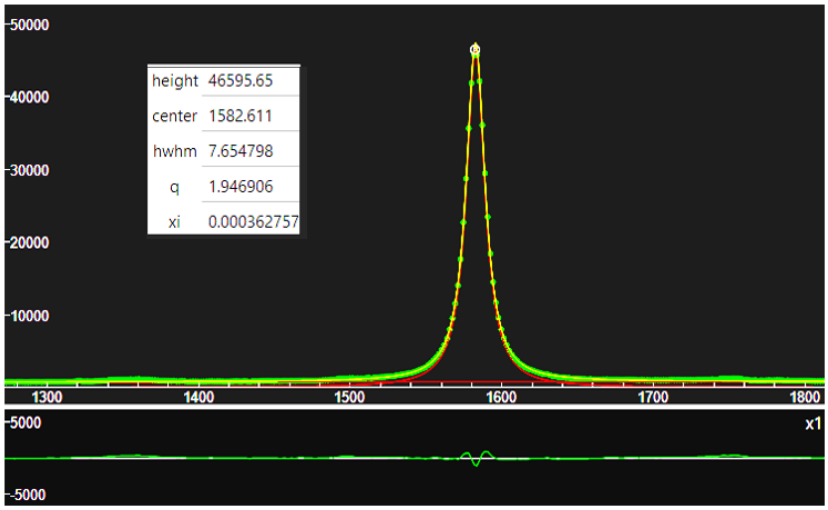

Fig. 21: The G band from a highly oriented pyrolytic graphite HOPG Raman spectrum kindly provided by Dmitrii Pudikov, CC BY 4.0, https://data.mendeley.com/datasets/rmtbjz5xjp/1 . The negligible value of parameter ξ is evidencing that the peak is symmetric. The value of q close to 2 is telling that the line is Lorentzian.

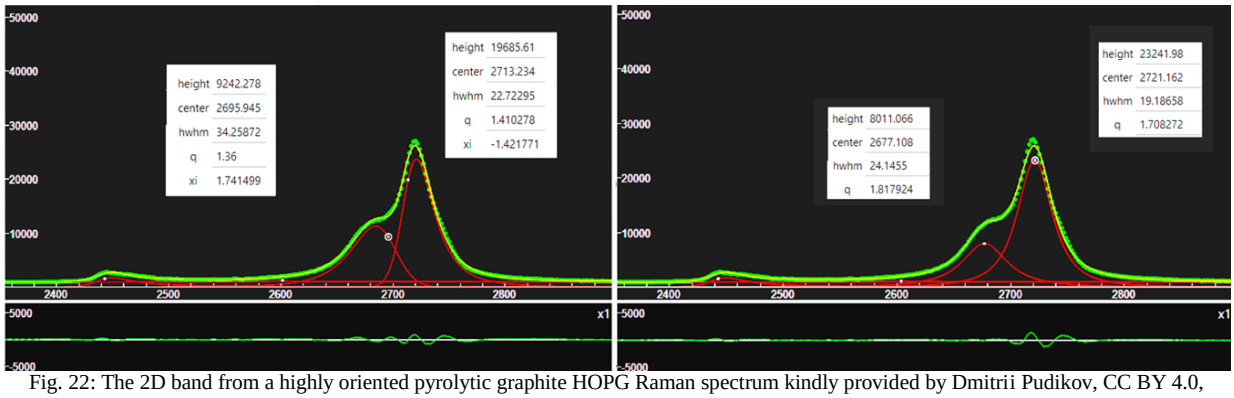

Fig. 22: The 2D band from a highly oriented pyrolytic graphite HOPG Raman spectrum kindly provided by Dmitrii Pudikov, CC BY 4.0, https://data.mendeley.com/datasets/rmtbjz5xjp/1 . The band is decomposed in two asymmetric components (q-BWFs, left panel) and in two symmetric components (q-Gaussians, right panel). The peaks are not Lorentzian.

In the Fig.22, we have very interesting decompositions of the 2D band in two q-BWF asymmetric functions and in two symmetric q-Gaussians. Further investigations on the use of q-BWF functions are necessary in order to assume their use as an effective manner to estimate both asymmetry and deviation from Lorentzian shape.

Appendix - Plasmons in general

Ukhtary and Saito, 2020, are helping us about plasmons. "Plasmon is collective oscillation of charge density in a metal in which the oscillation propagates in the direction of the wavevector q. Here *collective oscillation* means that free electrons in the metal oscillate in the same direction and phase to reduce the Coulomb repulsion between two electrons. Volume plasmon in three-dimensional (3D) metal is longitudinal oscillation of charge density in which the direction of the electric field is parallel to **q** … Since the longitudinal oscillation cannot be excited by transverse oscillation of electric field, the volume plasmon cannot be excited by a photon. On the other hand, surface plasmon is defined by the oscillation of charge density that propagates on the surface of a metal. In particular, for the case of two-dimensional (2D) graphene or one-dimensional (1D) carbon nanotube (CNT), since all carbon atoms exist on the surface, the plasmons in graphene and CNT are surface plasmons. In the case of surface plasmon, since the electric field induced by the charge density can be perpendicular to the surface, the surface plasmon can be excited by a photon. In solid state physics, the surface plasmon at the surface of 3D metal is often called a surface plasmon polariton in which the surface plasmon is coupled with electric polarization of a surrounding dielectric material" (Ukhtary and Saito, 2020).

Appendix – q-Gaussian, split-q-Gaussian and q-BWF functions

The q-Gaussian functions are probability distributions proper of the Tsallis statistics (Tsallis, 1988, Hanel et al., 2009). These functions are based on a generalized form of the exponential function, characterized by a continuous real parameter q. When q is going to 1, the q-exponential becomes the usual exponential function. The value q=2, (Naudts, 2009), corresponds to the Cauchy distribution, also known as the Lorentzian distribution; the q-Gaussian function is therefore a generalization of the Lorentzian distribution too. The change of q-parameter is allowing the q-Gaussian function to pass from the Gaussian to the Lorentzian distribution, in the form of a bell-shaped function with power-law wings ranging from Gaussian to Lorentzian tails.

As given by Umarov et al., 2008, the q-Gaussian function is: $f(x) = Ce_q(-\beta x^2)$, where $e_q(.)$ is the q-exponential function and C a constant (in the exponent, $\beta = 1/(2\sigma^2)$). The q-exponential has expression: $e_q(u) = [1 + (1-q)u]^{1/(1-q)}$. The plots in the Figures A.1 and A.2 are showing the behaviour of this exponential for different q values. Note that, for q less than one, the function is different from zero on a limited interval.

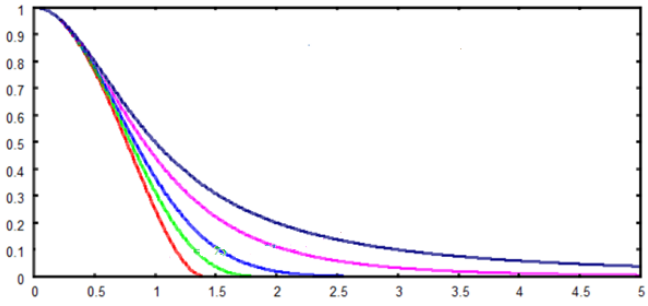

Fig.A.1: q- exponential functions, where the blue curve is representing a Lorentzian function (q=2). The pink curve corresponds to q=1.5 and light blue to q= 1.01, practically a Gaussian function. The green curve is the q-Gaussian for q=0.75 and red curve for q=0.5. For q < 1, the function is different from zero in a limited interval. Being the line symmetric, only the right side of it is given in the figure.

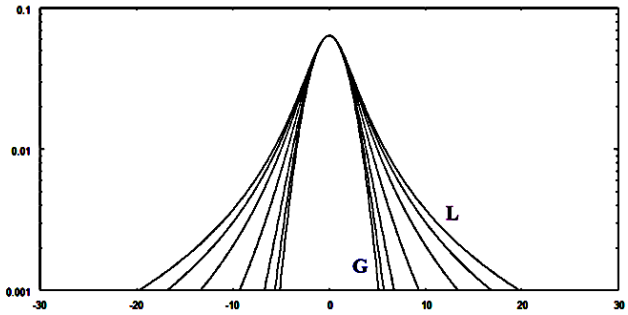

Fig.A.2: q-Gaussians, between the Lorentzian L and the Gaussian G function, in a log scale for the y-axis (semi log scale).

To have an asymmetric form of the q-Gaussian function, let us write it in the following manner (the center of the band is at x_o):

$$\text{q-Gaussian} = Cexp_q(-\beta(x-x_o)^2) = C[1-(1-q)\beta(x-x_o)^2]^{1/(1-q)}$$

In ChemRxiv we considered the asymmetric q-Gaussians, as given by Devi (2021):

$$\text{q-Gaussian}_{\text{LEFT}} = Cexp_{q_L}(-\beta_L(x-x_o)^2) = C[1-(1-q_L)\beta_L(x-x_o)^2]^{1/(1-q_L)}, \text{ when } x-x_o<0$$

$$\text{q-Gaussian}_{\text{RIGHT}} = Cexp_{q_R}(-\beta_R(x-x_o)^2) = C[1-(1-q_R)\beta_R(x-x_o)^2]^{1/(1-q_R)}, \text{ when } x-x_o>0$$

Parameters q and β of the Left and the Right parts are different. The most proper name for this asymmetric function is split-q-Gaussian. Moreover, we can generalize the Breit-Wigner-Fano into a q-Breit-Wigner-Fano.

In Fityk, a q-Gaussian function can be defined in the following manner:

define Qgau(height, center, hwhm, q=1.5) = height*(1+(q-1)*((x-center)/hwhm)^2)^(1/(1-q))

q=1.5 the initial guessed value of the q-parameter. Parameter hwhm is the half width at half maximum of the component. When q=2, the q-Gaussian is a Lorentzian function, that we can find defined in Fityk as:

Lorentzian(height, center, hwhm) = height/(1+((x-center)/hwhm)^2)

When q is close to 1, the q-Gaussian becomes a Gaussian function. The split q-Gaussian is defined as: Splitqgau(height, center, hwhm1=hwhm, hwhm2=hwhm, q1=1.5, q2=1.5) = x < center ? Qgau(height, center, hwhm1, q1) : Qgau(height, center, hwhm2, q2)

The split Lorentzian is: SplitLorentzian(height, center, hwhm1=hwhm, hwhm2=hwhm) = x < center ? Lorentzian(height, center, hwhm1) : Lorentzian(height, center, hwhm2)

The q-BWF can be defined as: Qbreit(height, center, hwhm, q=1.5, xi=0.1) = (1-xi*(q-1)*(x-center)/hwhm)^2 * height*(1+(q-1)^0.5 *((x-center)/hwhm)^2)^(1/(1-q))

And the BWF can be defined as: Breit(height, center, hwhm, xi=0.1) = (1-xi*(x-center)/hwhm)^2 * height/(1+((x-center)/hwhm)^2)

Let us note that the use of +xi instead of -xi does not change the fit in Fityk.

References

1. Athalin, H., & Lefrant, S. (2005). A correlated method for quantifying mixed and dispersed carbon nanotubes: analysis of the Raman band intensities and evidence of wavenumber shift. Journal of Raman Spectroscopy: An International Journal for Original Work in all Aspects of Raman Spectroscopy, Including Higher Order Processes, and also Brillouin and Rayleigh Scattering, 36(5), 400-408.
2. Antunes, E. F., Lobo, A. O., Corat, E. J., & Trava-Airoldi, V. J. (2007). Influence of diameter in the Raman spectra of aligned multi-walled carbon nanotubes. Carbon, 45(5), 913-921.
3. Basko, D. M., Piscanec, S., & Ferrari, A. C. (2009). Electron-electron interactions and doping dependence of the two-phonon Raman intensity in graphene. Physical Review B, 80(16), 165413.
4. Beyssac, O., Goffé, B., Chopin, C., & Rouzaud, J. N. (2002). Raman spectra of carbonaceous material in metasediments: a new geothermometer. Journal of metamorphic Geology, 20(9), 859-871.
5. Bokobza, L., Bruneel, J. L., & Couzi, M. (2015). Raman spectra of carbon-based materials (from graphite to carbon black) and of some silicone composites. C, 1(1), 77-94.
6. Brodie, B. C. (1860). Sur le poids atomique du graphite. Ann. Chim. Phys, 59(466), e472.
7. Brown, S. D. M., Jorio, A., Corio, A. P., Dresselhaus, M. S., Dresselhaus, G., Saito, R., & Kneipp, K. (2001). Origin of the Breit-Wigner-Fano lineshape of the tangential G-band feature of metallic carbon nanotubes. Physical Review B, 63(15), 155414.
8. Campbell, I. H., & Fauchet, P. M. (1986). The effects of microcrystal size and shape on the one phonon Raman spectra of crystalline semiconductors. Solid State Communications, 58(10), 739-741.
9. Cançado, L.G., Pimenta, M.A., Saito, R., Jorio, A., Ladeira, L.O., Grueneis, A., Souza-Filho, A.G., Dresselhaus, G., & Dresselhaus, M.S. (2002). Stokes and anti-Stokes double resonance Raman scattering in two-dimensional graphite. Physical Review B, 66(3), p.035415.
10. Childres, I., Jauregui, L. A., Park, W., Cao, H., & Chen, Y. P. (2013). Raman spectroscopy of graphene and related materials. New developments in photon and materials research, 1, 1-20.
11. Claramunt, S., Varea, A., Lopez-Diaz, D., Velázquez, M. M., Cornet, A., & Cirera, A. (2015). The importance of interbands on the interpretation of the Raman spectrum of graphene oxide. The Journal of Physical Chemistry C, 119(18), 10123- 10129.
12. Cui, L., & Sun, M. (2021). Graphene plasmon-enhanced polarization-dependent interfacial charge transfer excitons in 2D graphene-black phosphorus heterostructures in NIR and

MIR regions. The Journal of Physical Chemistry C, 125(40), 22370-22378.
13. Devi, S. (2021). Asymmetric Tsallis distributions for modeling financial market dynamics. Physica A: Statistical Mechanics and Its Applications, 578, 126109
14. Dikin, D. A., Stankovich, S., Zimney, E. J., Piner, R. D., Dommett, G. H., Evmenenko, G., Nguyen, S. T., & Ruoff, R. S. (2007). Preparation and characterization of graphene oxide paper. Nature, 448(7152), pp.457-460.
15. Di Tinno, A., Cancelliere, R., Mantegazza, P., Cataldo, A., Paddubskaya, A., Ferrigno, L., Kuzhir, P., Maksimenko, S., Shuba, M., Maffucci, A., & Bellucci, S. (2022). Sensitive detection of industrial pollutants using modified electrochemical platforms. Nanomaterials, 12(10), p.1779.
16. Dresselhaus, M. S., & Eklund, P. C. (2000). Phonons in carbon nanotubes. Advances in physics, 49(6), 705-814.
17. Dresselhaus, M. S., Dresselhaus, G., Jorio, A., Souza Filho, A. G., & Saito, R. (2002). Raman spectroscopy on isolated single wall carbon nanotubes. Carbon, 40(12), 2043-2061.
18. Dresselhaus, M. S., & Dresselhaus, G. (1981). Intercalation compounds of graphite. Advances in Physics, 30(2), 139-326.
19. Dresselhaus, M. S., Dresselhaus, G., Jorio, A., AG Filho, S., Samsonidze, G. G., & Saito, R. (2003). Science and applications of single-nanotube Raman spectroscopy. Journal of nanoscience and nanotechnology, 3(1-2), 19-37.
20. Dresselhaus, M. S., Dresselhaus, G., Saito, R., & Jorio, A. (2005). Raman spectroscopy of carbon nanotubes. Physics reports, 409(2), 47-99.
21. Dubay, O., Kresse, G., & Kuzmany, H. (2002). Phonon softening in metallic nanotubes by a Peierls-like mechanism. Physical review letters, 88(23), 235506.
22. Ejehi, F., Mohammadpour, R., Asadian, E., Sasanpour, P., Fardindoost, S., & Akhavan, O. (2020). Graphene oxide papers in nanogenerators for self-powered humidity sensing by finger tapping. Scientific reports, 10(1), 7312.
23. Enoki, T., Suzuki, M., & Endo, M. (2003). Graphite intercalation compounds and applications. Oxford University Press.
24. Fenske, M. R., Braun, W. G., Wiegand, R. V., Quiggle, D., McCormick, R., & Rank, D. H. (1947). Raman spectra of hydrocarbons. Analytical Chemistry, 19(10), 700-765.
25. Ferrari, A. C. (2007). Raman spectroscopy of graphene and graphite: Disorder, electron–phonon coupling, doping and nonadiabatic effects. Solid state communications, 143(1-2), 47-57.
26. Ferrari, A. C., & Basko, D. M. (2013). Raman spectroscopy as a versatile tool for studying the properties of graphene. Nature nanotechnology, 8(4), 235-246.
27. Ferrari, A. C., Meyer, J. C., Scardaci, V., Casiraghi, C., Lazzeri, M., Mauri, F., Piscanec, S., Jiang, D., Novoselov, K. S., Roth, S., & Geim, A. K. (2006). Raman spectrum of graphene and graphene layers. Physical Review Letters 97: 187401.
28. Ferrari, A. C., & Robertson, J. (2000). Interpretation of Raman spectra of disordered and amorphous carbon. Physical Review B 61: 14095–14107.
29. Frisenda, R., Niu, Y., Gant, P., Muñoz, M., & Castellanos-Gomez, A. (2020). Naturally occurring van der Waals materials. npj 2D Materials and Applications, 4(1), 38.
30. Gavilan, L., Ricketts, C. L., Bejaoui, S., Ricca, A., Boersma, C., Salama, F., & Mattioda, A. L. (2022). Raman spectroscopic study of pyrene in cosmic dust analogues: evolution from the gas to the solid phase. ACS Earth and Space Chemistry, 6(9), 2215-2225.
31. Geim, A. K., & Novoselov, K. S. (2007). The rise of graphene. Nature materials, 6(3), 183-191.
32. Goldie, S. J., Bush, S., Cumming, J. A., & Coleman, K. S. (2020). A statistical approach to Raman analysis of graphene-related materials: implications for quality control. ACS Applied Nano Materials, 3(11), 11229-11239.
33. Gupta, A., Chen, G., Joshi, P., Tadigadapa, S., & Eklund, P. C. (2006). Raman scattering from high-frequency phonons in supported n-graphene layer films. Nano letters, 6(12), 2667-2673.
34. Haidari, M. M., Kim, H., Kim, J. H., Park, M., Lee, H., & Choi, J. S. (2020). Doping effect in graphene-graphene oxide interlayer. Scientific Reports, 10(1), 8258.
35. Hanel, R., Thurner, S., & Tsallis, C. (2009). Limit distributions of scale-invariant probabilistic models of correlated random variables with the q-Gaussian as an explicit example. The European Physical Journal B, 72(2), 263.
36. Hasdeo, E. H., Nugraha, A. R., Dresselhaus, M. S., & Saito, R. (2014). Breit-Wigner-Fano line shapes in Raman spectra of graphene. Physical Review B, 90(24), 245140.
37. Heid, R. (2017). Electron-Phonon Coupling. In The Physics of Correlated Insulators, Metals, and Superconductors. Vol.7. Pavarini, E., Koch, E., Scalettar, R. and Martin, R. (eds.). Verlag des Forschungszentrum Jülich, 2017, ISBN 978-3-95806-224-5 Open access. Available https://www.cond-mat.de/events/correl17/manuscripts/
38. Heise, H. M., Kuckuk, R., Ojha, A. K., Srivastava, A., Srivastava, V., & Asthana, B. P. (2009). Characterisation of carbonaceous materials using Raman spectroscopy: a comparison of carbon nanotube filters, single-and multi-walled nanotubes, graphitised porous carbon and graphite. Journal of Raman Spectroscopy: An International Journal for Original Work in all Aspects of Raman Spectroscopy, Including Higher Order Processes, and also Brillouin and Rayleigh Scattering, 40(3), 344-353.
39. Hummers, W., & Offeman, R. (1958). Preparation of graphitic oxide. J. Am. Chem. Soc. 80, 1339.
40. Jiang, C., Kempa, K., Zhao, J., Schlecht, U., Kolb, U., Basché, T., Burghard, M., & Mews, A. (2002). Strong enhancement of the Breit-Wigner-Fano Raman line in carbon nanotube bundles caused by plasmon band formation. Physical Review B, 66(16), p.161404.
41. Jorio, A., Saito, R., Hafner, J.H., Lieber, C.M., Hunter, D.M., McClure, T., Dresselhaus, G., & Dresselhaus, M.S. (2001). Structural (n, m) determination of isolated single-wall carbon nanotubes by resonant Raman scattering. Physical review letters, 86(6), p.1118.
42. Jorio, A., Pimenta, M. A., Souza Filho, A. G., Saito, R., Dresselhaus, G., & Dresselhaus, M. S. (2003). Characterizing carbon nanotube samples with resonance Raman scattering. New Journal of Physics, 5(1), 139.
43. Jorio, A., Dresselhaus, M., Saito, R., & Dresselhaus, G. F. (2011). Raman Spectroscopy in Graphene Related Systems; WILEY-VCH Verlag GmbH& Co. KGaA: Weinheim, Germany
44. Jorio, A., & Saito, R. (2021). Raman spectroscopy for carbon nanotube applications. Journal of Applied Physics, 129(2).
45. Kang, D., Kato, K., Kojima, K., Uchida, T., & Tachibana, M. (2008). Phonon control in metallic carbon nanotubes due to laser-induced defects. Applied Physics Letters, 93(13).
46. Kempa, K. (2002). Gapless plasmons in carbon nanotubes and their interactions with phonons. Physical Review B, 66(19), 195406.
47. King, A. A. K., Davies, B. R., Noorbehesht, N., Newman, P., Church, T.L., Harris, A. T., Razal, J. M., & Minett, A. I. (2016). A new Raman metric for the characterisation of graphene oxide and its derivatives. Scientific Reports 6(1),1–6, http://dx.doi.org/10.1038/srep19491.
48. Knight, D. S., & White, W. B. (1989). Characterization of diamond films by Raman spectroscopy. Journal of Materials Research, 4, 385-393.
49. Krishnan, R. S. (1945). Raman spectrum of diamond. Nature, 155(3928), 171-171.
50. Krupke, R., Hennrich, F., Lohneysen, H. V., & Kappes, M. M. (2003). Separation of metallic from semiconducting single-walled carbon nanotubes. Science, 301(5631), 344-347.
51. Kürti, J., Zólyomi, V., Grüneis, A., & Kuzmany, H. (2002). Double resonant Raman phenomena enhanced by van Hove singularities in single-wall carbon nanotubes. Physical Review B, 65(16), 165433.
52. Kuzmenko, A.B., Benfatto, L., Cappelluti, E., Crassee, I., Van Der Marel, D., Blake, P., Novoselov, K.S., & Geim, A.K. (2009). Gate tunable infrared phonon anomalies in bilayer graphene. Physical review letters, 103(11), p.116804.
53. Lazzeri, M., Piscanec, S., Mauri, F., Ferrari, A. C., & Robertson, J. (2006). Phonon linewidths and electron-phonon coupling in graphite and nanotubes. Physical review B, 73(15), 155426.

54. Lerf, A., He, H., Forster, M., & Klinowski, J. (1998). Structure of Graphite Oxide Revisited. J. Phys. Chem. B,102, 4477−4482
55. Li, Z., Deng, L., Kinloch, I. A., & Young, R. J. (2023). Raman spectroscopy of carbon materials and their composites: Graphene, nanotubes and fibres. Progress in Materials Science, 135, 101089.
56. Lin-Vien, D., Colthup, N. B., Fateley, W. G., & Grasselli, J. G. (1991). The handbook of infrared and Raman characteristic frequencies of organic molecules. Elsevier.
57. Liu, Y. H., Ma, Z. K., He, Y., Wang, Y., Zhang, X. W., Song, H. H., & Li, C. X. (2023). A review of fibrous graphite materials: graphite whiskers, columnar carbons with a cone-shaped top, and needle-and rods-like polyhedral crystals. New Carbon Materials, 38(1), 18-35.
58. Lucchese, M.M., Stavale, F., Ferreira, E.M., Vilani, C., Moutinho, M.V.D.O., Capaz, R.B., Achete, C.A., & Jorio, A. (2010). Quantifying ion-induced defects and Raman relaxation length in graphene. Carbon, 48(5), pp.1592-1597.
59. Malard, L. M., Pimenta, M. A., Dresselhaus, G., & Dresselhaus, M. S. (2009). Raman spectroscopy in graphene. Physics reports, 473(5-6), 51-87.
60. Mapelli, C. (1998). Tesi di Laurea, Politecnico di Milano.
61. Mapelli, C., Castiglioni, C., Zerbi, G., & Müllen, K. (1999). Common force field for graphite and polycyclic aromatic hydrocarbons. Physical Review B, 60(18), 12710.
62. Maultzsch, J. (2004). Vibrational properties of carbon nanotubes and graphite, Ph.D. thesis, Technische Universität Berlin, Berlin.
63. Merlen, A., Buijnsters, J. G., & Pardanaud, C. (2017). A guide to and review of the use of multiwavelength Raman spectroscopy for characterizing defective aromatic carbon solids: From graphene to amorphous carbons. Coatings, 7(10), 153.
64. Milani, A., Tommasini, M., Russo, V., Bassi, A. L., Lucotti, A., Cataldo, F., & Casari, C. S. (2015). Raman spectroscopy as a tool to investigate the structure and electronic properties of carbon-atom wires. Beilstein journal of nanotechnology, 6(1), 480-491.
65. Miroshnichenko, A. E., Flach, S., & Kivshar, Y. S. (2010). Fano resonances in nanoscale structures. Reviews of Modern Physics, 82(3), 2257.
66. Mishra A.K., & Ramaprabhu, S. (201). Hybrid carbon nanostructure assemblage for high performance pseudo-capacitors. AIP Adv. 2, http://dx.doi.org/10.1063/1.4717490.
67. Mu, X., & Sun, M. (2020). The linear and non-linear optical absorption and asymmetrical electromagnetic interaction in chiral twisted bilayer graphene with hybrid edges. Materials Today Physics, 14, 100222. 10.1016/j.mtphys.2020.100222.
68. Naudts, J. (2009). The q-exponential family in statistical physics. Central European Journal of Physics, 7, 405-413.
69. Nemanich, R. J., Solin, S. A., & Martin, R. M. (1981). Light scattering study of boron nitride microcrystals. Physical Review B, 23(12), 6348.
70. Novoselov, K.S., Geim, A.K., Morozov, S.V., Jiang, D.E., Zhang, Y., Dubonos, S.V., Grigorieva, I.V., & Firsov, A.A. (2004). Electric field effect in atomically thin carbon films. science, 306(5696), pp.666-669.
71. O'Brien, C. (2023). Graphene Market & 2D Materials Assessment 2024-2034: Technologies, Markets, Players. IDTechEx ISBN 9781915514967
72. Osswald, S., Havel, M., & Gogotsi, Y. (2007). Monitoring oxidation of multiwalled carbon nanotubes by Raman spectroscopy. Journal of Raman Spectroscopy: An International Journal for Original Work in all Aspects of Raman Spectroscopy, Including Higher Order Processes, and also Brillouin and Rayleigh Scattering, 38(6), 728-736.
73. Ott, A. K., & Ferrari, A. C. (2024). Raman spectroscopy of graphene and related materials. Encyclopedia of Condensed Matter Physics, 2nd ed.; Chakraborty, T., Ed, 233-247.
74. Paillet, M., Poncharal, P., Zahab, A., Sauvajol, J. L., Meyer, J. C., & Roth, S. (2005). Vanishing of the Breit-Wigner-Fano component in individual single-wall carbon nanotubes. Physical review letters, 94(23), 237401.
75. Pimenta, M.A., Marucci, A., Empedocles, S.A., Bawendi, M.G., Hanlon, E.B., Rao, A.M., Eklund, P.C., Smalley, R.E., Dresselhaus, G., & Dresselhaus, M.S. (1998). Raman modes of metallic carbon nanotubes. Physical Review B, 58(24), p.R16016.
76. Pudikov, D. (2017). Experimental data and supporting information for "Graphene fabrication via carbon segregation through transition metal films", Mendeley Data, V1, doi: 10.17632/rmtbjz5xjp.1
77. Pudikov, D. A., Zhizhin, E. V., Rybkin, A. G., & Shikin, A. M. (2018). Graphene fabrication via carbon segregation through transition metal films. Thin Solid Films, 648, 120-127.
78. Rao, A. M., Jorio, A., Pimenta, M. A., Dantas, M. S. S., Saito, R., Dresselhaus, G., & Dresselhaus, M. S. (2000). Polarized Raman study of aligned multiwalled carbon nanotubes. Physical review letters, 84(8), 1820.
79. Rautian, S. G. (1958). Real spectral apparatus. Soviet Physics Uspekhi, 1(2), 245
80. Richter, H., Wang, Z. P., & Ley, L. (1981). The one phonon Raman spectrum in microcrystalline silicon. Solid State Communications, 39(5), 625-629.
81. Reich, S., Thomsen, C., Duesberg, G. S., & Roth, S. (2001). Intensities of the Raman-active modes in single and multiwall nanotubes. Physical Review B, 63(4), 041401.
82. Sadezky, A., Muckenhuber, H., Grothe, H., Niessner, R., & Pöschl, U. (2005). Raman microspectroscopy of soot and related carbonaceous materials: Spectral analysis and structural information. Carbon, 43(8), 1731-1742.
83. Saito, R., Hofmann, M., Dresselhaus, G., Jorio, A., & Dresselhaus, M. S. (2011). Raman spectroscopy of graphene and carbon nanotubes. Advances in Physics, 60(3), 413-550.
84. Sardinha, A. (2019). Raman spectra of Graphene oxide, Mendeley Data, V1, doi: 10.17632/n4nts7hvvx.1
85. Sardinha, A. (2019), Raman spectra of Graphene oxide, Mendeley Data, V2, doi: 10.17632/n4nts7hvvx.2
86. Sardinha, A. F., Almeida, D. A., & Ferreira, N. G. (2020). Electrochemical impedance spectroscopy correlation among graphene oxide/carbon fibers (GO/CF) composites and GO structural parameters produced at different oxidation degrees. Journal of Materials Research and Technology, 9(5), 10841-10853.
87. Schniepp, H.C., Li, J.L., McAllister, M.J., Sai, H., Herrera-Alonso, M., Adamson, D.H., Prud'homme, R.K., Car, R., Saville, D.A., & Aksay, I.A. (2006). Functionalized single graphene sheets derived from splitting graphite oxide. The journal of physical chemistry B, 110(17), pp.8535-8539.
88. Seshadri, K., & Jones, R. N. (1963). The shapes and intensities of infrared absorption bands—A review. Spectrochimica Acta, 19(6), 1013-1085
89. Shuker, R., & Gammon, R. W. (1970). Raman-scattering selection-rule breaking and the density of states in amorphous materials. Physical Review Letters, 25(4), 222.
90. Siklitskaya, A., Gacka, E., Larowska, D., Mazurkiewicz-Pawlicka, M., Malolepszy, A., Stobiński, L., Marciniak, B., Lewandowska-Andrałojć, A., & Kubas, A. (2021). Lerf–Klinowski-type models of graphene oxide and reduced graphene oxide are robust in analyzing non-covalent functionalization with porphyrins. Scientific reports, 11(1), p.7977.
91. Sousa, D. V. D., Guimarães, L. M., Felix, J. F., Ker, J. C., Schaefer, C. E. R., & Rodet, M. J. (2020). Dynamic of the structural alteration of biochar in ancient Anthrosol over a long timescale by Raman spectroscopy. PloS one, 15(3), e0229447.
92. Sparavigna, A. C. (2023). q-Gaussian Tsallis Line Shapes and Raman Spectral Bands. Int. J. Sciences, 12(3), 27-40, 2023, http://dx.doi.org/10.18483/ijSci.2671
93. Sparavigna, A. C. (2023). q-Gaussian Tsallis Line Shapes for Raman Spectroscopy (June 7, 2023). SSRN Electronic Journal. http://dx.doi.org/10.2139/ssrn.4445044
94. Sparavigna, A. C. (2023). SERS Spectral Bands of L-Cysteine, Cysteamine and Homocysteine Fitted by Tsallis q-Gaussian Functions. International Journal of Sciences, 12(09), 14–24. https://doi.org/10.18483/ijsci.2721
95. Sparavigna, A. C. (2024). Raman Spectroscopy of Siderite with q-Gaussian and split-q-Gaussian Analyses. International Journal of Sciences, 13(02), 8-21.
96. Sparavigna, A. C. (2024). Pyrene and Biochar (Raman Spectroscopy). ChemRxiv. doi:10.26434/chemrxiv-2024-

7zbtf
97. Sparavigna, A. C. (2024). Molybdenum Disulfide MoS2 and the q-BWF line shapes (Raman Spectroscopy). ChemRxiv. doi:10.26434/chemrxiv-2024-cprs3-v3
98. Stankovich, S., Dikin, D.A., Piner, R.D., Kohlhaas, K.A., Kleinhammes, A., Jia, Y., Wu, Y., Nguyen, S.T., & Ruoff, R.S. (2007). Synthesis of graphene-based nanosheets via chemical reduction of exfoliated graphite oxide. carbon, 45(7), pp.1558-1565.
99. Stankovich, S., Piner, R.D., Chen, X., Wu, N., Nguyen, S.T., & Ruoff, R.S. (2006). Stable aqueous dispersions of graphitic nanoplatelets via the reduction of exfoliated graphite oxide in the presence of poly (sodium 4-styrenesulfonate). Journal of Materials Chemistry, 16(2), pp.155-158.
100. Stankovich, S., Piner, R.D., Nguyen, S.T., & Ruoff, R.S. (2006). Synthesis and exfoliation of isocyanate-treated graphene oxide nanoplatelets. Carbon, 44(15):3342–7.
101. Stankovich, S., Dikin, D.A., Dommett, G.H., Kohlhaas, K.M., Zimney, E.J., Stach, E.A., Piner, R.D., Nguyen, S.T. , & Ruoff, R.S. (2006). Graphene-based composite materials. nature, 442(7100), pp.282-286.
102. Staudenmaier, L. (1898). Verfahren zur darstellung der graphitsäure. Berichte der deutschen chemischen Gesellschaft, 31(2), 1481-1487.
103. Staudenmaier, L. (1899). Verfahren zur darstellung der graphitsäure. Berichte der deutschen chemischen Gesellschaft, 32(2), 1394-1399.
104. Strano, M.S., Dyke, C.A., Usrey, M.L., Barone, P.W., Allen, M.J., Shan, H., Kittrell, C., Hauge, R.H., Tour, J.M., & Smalley, R.E. (2003). Electronic structure control of single-walled carbon nanotube functionalization. Science, 301(5639), pp.1519-1522.
105. Tachibana, M. (2013). Characterization of laser-induced defects and modification in carbon nanotubes by Raman spectroscopy. Physical and chemical properties of carbon nanotubes, 31-52, Satoru Suzuki Editor. https://www.intechopen.com/chapters/38953
106. Tan, P., Hu, C., Dong, J., Shen, W., & Zhang, B. (2001). Polarization properties, high-order Raman spectra, and frequency asymmetry between Stokes and anti-Stokes scattering of Raman modes in a graphite whisker. Physical Review B, 64(21), 214301.
107. Tang, T.T., Zhang, Y., Park, C.H., Geng, B., Girit, C., Hao, Z., Martin, M.C., Zettl, A., Crommie, M.F., Louie, S.G., & Shen, Y.R. (2010). A tunable phonon–exciton Fano system in bilayer graphene. Nature nanotechnology, 5(1), pp.32-36.
108. Telg, H., Maultzsch, J., Reich, S., & Thomsen, C. (2005). Chirality dependence of the high-energy Raman modes in carbon nanotubes. In AIP Conference Proceedings (Vol. 786, No. 1, pp. 162-165). American Institute of Physics.
109. Telg, H., Fouquet, M., Maultzsch, J., Wu, Y., Chandra, B., Hone, J., Heinz, T.F., & Thomsen, C. (2008). G^- and G^+ in the Raman spectrum of isolated nanotube: a study on resonance conditions and lineshape. physica status solidi (b), 245(10), pp.2189-2192.
110. Thomsen, C., & Reich, S. (2000) Double resonant Raman scattering in graphite. Physical Review Letters 85: 5214–5217.
111. Thomsen, C., & Reich, S. (2007). Raman scattering in carbon nanotubes. Light Scattering in Solid IX, 115-234.
112. Tsallis, C. (1988). Possible generalization of Boltzmann-Gibbs statistics. Journal of statistical physics, 52, 479-487.
113. Tuinstra, F., & Koenig, J. L. (1970) Raman spectrum of graphite. The Journal of Chemical Physics 53, 1126–1130.
114. Uchida, T., Tachibana, M., Kurita, S., & Kojima, K. (2004). Temperature dependence of the Breit–Wigner–Fano Raman line in single-wall carbon nanotube bundles. Chemical physics letters, 400(4-6), 341-346.
115. Ukhtary, M. S., & Saito, R. (2020). Surface plasmons in graphene and carbon nanotubes. Carbon, 167, 455-474.
116. Umarov, S., Tsallis, C., & Steinberg, S. (2008). On a q-Central Limit Theorem Consistent with Nonextensive Statistical Mechanics. Milan J. Math. Birkhauser Verlag. 76: 307–328. doi:10.1007/s00032-008-0087-y. S2CID 55967725.
117. Wojdyr, M. (2010). Fityk: a general-purpose peak fitting program. Journal of Applied Crystallography, 43(5-1), 1126-1128.
118. Wu, J. B., Lin, M. L., Cong, X., Liu, H. N., & Tan, P. H. (2018). Raman spectroscopy of graphene-based materials and its applications in related devices. Chemical Society Reviews, 47(5), 1822-1873.
119. Yogi, P., Saxena, S.K., Mishra, S., Rai, H.M., Late, R., Kumar, V., Joshi, B., Sagdeo, P.R., & Kumar, R. (2016). Interplay between phonon confinement and Fano effect on Raman line shape for semiconductor nanostructures: analytical study. Solid State Communications, 230, pp.25-29.
120. Yoon, D., Jeong, D., Lee, H. J., Saito, R., Son, Y. W., Lee, H. C., & Cheong, H. (2013). Fano resonance in Raman scattering of graphene. Carbon, 61, 373-378.
121. Zhang, C. C., Hartlaub, S., Petrovic, I., & Yilmaz, B. (2022). Raman spectroscopy characterization of amorphous coke generated in industrial processes. ACS omega, 7(3), 2565-2570.
122. Zhao, X., Ando, Y., Qin, L. C., Kataura, H., Maniwa, Y., & Saito, R. (2002). Multiple splitting of G-band modes from individual multiwalled carbon nanotubes. Applied physics letters, 81(14), 2550-2552.
123. Zheng, M., Jagota, A., Strano, M.S., Santos, A.P., Barone, P., Chou, S.G., Diner, B.A., Dresselhaus, M.S., Mclean, R.S., Onoa, G.B., & Samsonidze, G.G. (2003). Structure-based carbon nanotube sorting by sequence-dependent DNA assembly. Science, 302(5650), pp.1545-1548.